공학석사 학위논문

Frequency-domain FWI for 2D VTI media using pseudo-acoustic and pure-acoustic wave equations

유사 음향 파동 방정식과 순수 음향 파동 방정식을 이용한 2차원 VTI매질에 대한 주파수 영역에서의 완전파형역산

2015 년 8 월

서울대학교 대학원

에너지시스템공학부

진 효 준

Frequency-domain FWI for 2D VTI media using pseudo-acoustic and pure-acoustic wave equations

유사 음향 파동 방정식과 순수 음향 파동 방정식을 이용한
2차원 VTI매질에 대한 주파수 영역에서의 완전파형역산

지도 교수 신 창 수

이 논문을 공학석사 학위논문으로 제출함
2015년 5 월

서울대학교 대학원
에너지시스템공학부
진 효 준

진효준의 공학석사 학위논문을 인준함
2015 년 6 월

위 원 장 _____ **(인)**

부위원장 _____ **(인)**

위 원 _____ **(인)**

Abstract

Describing the exact wavefield movement is required to obtain a more accurate subsurface velocity model during full waveform inversion (FWI). Real rock environments are composed of many anisotropy factors, but the conventional FWI assumes that the subsurface is an isotropic medium. Because of these assumptions, it is difficult to describe realistic wavefield motion. This is not sufficient to obtain the appropriate subsurface velocity model.

To more closely simulate realistic wavefield motion, we selected the pseudo-acoustic wave equation and the pure-acoustic wave equation suggested by Fletcher et al., 2009, and Chu et al., 2011. When we apply both equations to FWI, a large difference in performance is expected because both equations have different formulations. One of the important considerations in the multiparameter FWI is the radiation pattern of the parameters. The radiation pattern can be calculated using a partial derivative wavefield, and many researchers have proposed that setting the parameters that do not influence the other parameters is good for parameterization when analyzing the radiation patterns.

We simulated both equations in the frequency-domain, and we calculated the radiation patterns of P-wave, epsilon, and delta in the time-domain. To determine whether the behavior is good and the possibility of the two algorithms, we tested synthetic data generated in the frequency-domain using the same equation and modeling scheme. Considering a more realistic situation, we generated a synthetic dataset under the time-domain using an elastic wave equation with a marine environment assumption and applied two algorithms. The tests of the time-domain synthetic dataset used 6 cases of initial models and updating strategies. Additionally, we applied conventional isotropy FWI to

the same synthetic dataset and calculated the relative percentage errors between the true model and the inverted model. Through the relative percentage errors called model misfits, we compared the performance of conventional FWI with the proposed FWI. Finally, we applied both algorithms to the 2D TTI model officially provided by “BP Exploration Operation Company”, and reconfirmed the importance of anisotropy factors.

Keywords: Frequency-domain full waveform inversion, Anisotropy parameters, Pseudo-acoustic wave, Pure-acoustic wave

Student Number : 2013-23186

Contents

List of Figures

List of Tables

Chapter 1 Introduction

Waveform inversion has been used as a reasonable tool for extracting subsurface parameters using pre-stack seismic data since the development of the adjoint method by Lailly (1983) and Tarantola (1984). Over the past 30 years, seismic inversion has experienced considerable development with the advancements in seismic exploration theories and computational environments (Tarantola, 1984; Mora, 1987; Bunks et al., 1995; Pratt et al., 1998; Operto et al., 2004; Shin et al., 2007; Shin and Cha, 2008, 2009).

Although the development of the adjoint method proposed the possibility of a waveform inversion algorithm, the realistic application of the waveform inversion still faces some difficulties. The first problem is the massive computational costs. To calculate the forward and backward wavefields, we need to solve the impedance matrix related to the model parameters. For the two-dimensional case, Trefethen and Bau implemented an iterative matrix solver in 1997, and Kim and Kim developed a very efficient computational approach, the direct solver, in 1999. However, to resolve the three-dimensional case, the required computational resources would be dramatically increased. Because the direct matrix solver requires saving LU factors in RAM (random access memory) or on a hard disk, the iterative solver is widely used for solving the three-dimensional problem (Operto et al., 2007). Thus, considerable work remains. Ben-Hadj-Ali et al. (2008) performed acoustic FWI in the frequency-domain by solving the forward problem with a frequency-domain finite difference method based on a massively parallel direct solver,. Plessix (2009) used the iterative solver with a multigrid preconditioner to perform three-dimensional frequency domain FWI, and Kim et al. (2013) used Sirgue et al.

(2008)'s approach and applied it to the three-dimensional Laplace-Fourier domain acoustic FWI.

The second problem is the non-linearity of the inverse problem. FWI is considered to be a non-linear problem because the local minimum points exist in the objective function. The problem of non-linearity becomes more severe when the initial model is far from the true model (Gauthier et al., 1986). To overcome the non-linearity problem, Bunks et al. (1995) proposed a multiscale approach to the seismic inversion problem and reduced local minima by using the multigrid method. Shipp and Singh (2002) and Sirgue and Pratt (2004) selected a starting model that is similar to the real model to escape the problem of local minima. Furthermore, a few approaches that use robust objective functions have been proposed to overcome the non-linearity inverse problems. Guitton and Symes (2003) applied Huber norm to the noisy seismic data inversion. Shin and Min (2006) suggested the logarithmic objective function. Shin and Cha (2008) developed Laplace-domain FWI and it can provide a background P-wave velocity model even though the seismic data have no low frequency components.

Additionally, it is difficult to perfectly represent seismic wave propagation through numerical simulations because real earth media contain many unknown factors and complexities. For this reason, it is difficult to reconstruct accurate subsurface information through seismic waveform inversion. Recently, many researchers have been concentrating on the multiple parameters of the subsurface media: P- and S-wave velocities, density, anisotropy parameters, and attenuation (Q-factor). In the early stages of the FWI, the majority of classical studies only considered P-wave velocity with the isotropic acoustic wave equation (Laily, 1983; Tarantola, 1984; Kolb et al., 1986; Gauthier et al.,

1986; Pratt et al., 1998). With the development of equipment and techniques, obtaining multi-component data has become common in recent years, and thus, FWI based on the elastic wave equation has emerged, which strives for the reconstruction of multiparameter (Mora 1987; Choi et al., 2008; Brossier et al., 2009). Furthermore, the importance of anisotropy has been taken into account in seismic data processing. In the RTM (reverse time migration) processing field, which considers the anisotropy factors, many researchers have already developed RTM algorithms associated with anisotropic factors, which have provided better subsurface images than conventional isotropic RTM (Duveneck et al., 2008; Fowler et al., 2008; Fletcher et al., 2009; Kim et al., 2013). Moreover, many studies of FWI have also considered anisotropy, particularly vertical transverse isotropic media (Lee et al., 2010; Plessix and Cao, 2011; Gholami et al., 2013a, 2013b). Thus, considering the anisotropy properties of subsurface media is a major issue in seismic data processing.

Because of the aforementioned reasons, to obtain more precise results with FWI in anisotropic media, we applied the pseudo-acoustic wave equation and pure-acoustic wave equation to multiparameter FWI. In this paper, we first briefly review the pseudo-acoustic, and pure-acoustic wave propagation modeling in the frequency-domain using the finite-element method and frequency-domain FWI. Second, we simulate the radiation patterns and analyze the results. Third, to verify the two proposed algorithms, which are the pseudo-acoustic wave equation and the pure-acoustic wave equation, we test waveform inversion under forward modeling and backward modeling using same modeling algorithm. Fourth, we apply the proposed frequency-domain FWI to Overthrust 2D VTI synthetic data and discuss the performance of this algorithm. Finally, we emphasize why we consider the anisotropy parameters during FWI processing using an officially published dataset, BP TTI synthetic dataset.

Chapter 2 Theory

2.1 The pseudo-acoustic and pure-acoustic wave equations in the frequency-domain

Solving the Christoffel equations for homogeneous TTI(tilted transversely isotropic) media provides three distinct wave modes: P, SV, and SH(Tsvankin, 2001). The dispersion relation for P-SV waves in TTI media is (Fletcher et al., 2009)

$$\begin{aligned}\omega^4 = &\left[\left(v_{px}^2 + v_{sz}^2\right)\left(\widehat{k_x^2} + \widehat{k_y^2}\right) + \left(v_{pz}^2 + v_{sz}^2\right)\widehat{k_z^2}\right]\omega^2 - v_{px}^2 v_{sz}^2\left(\widehat{k_x^2} + \widehat{k_y^2}\right)^2 \\ &- v_{pz}^2 v_{sz}^2 \widehat{k_z^4} + \left[v_{pz}^2\left(v_{pn}^2 - v_{px}^2\right) - v_{sz}^2\left(v_{pn}^2 + v_{pz}^2\right)\right] \\ &\times \left(\widehat{k_x^2} + \widehat{k_y^2}\right)\widehat{k_z^2}\end{aligned}$$

(2.1.1)

where ω is the angular frequency, v_{pz} is the P-wave velocity along the symmetry axis, $v_{pn} = v_{pz}\sqrt{1+2\delta}$ is the P-wave moveout velocity relative to the symmetry axis, $v_{px} = v_{pz}\sqrt{1+2\epsilon}$ is the P-wave velocity perpendicular to the symmetry axis, v_{sz} is the SV-wave velocity along the symmetry axis, ϵ and δ are Thomsen's anisotropy parameters, and $\widehat{k_x}$, $\widehat{k_y}$, and $\widehat{k_z}$ are spatial wavenumbers, which are evaluated in a rotated coordinate system aligned with the axis of symmetry. Specifically,

$$\widehat{k_x} = k_x cos\theta cos\phi + k_y cos\theta sin\phi - k_z sin\theta$$

$$\widehat{k_y} = -k_x sin\phi + k_y cos\phi$$

$$\widehat{k_z} = k_x sin\theta cos\phi + k_y sin\theta sin\phi + k_z cos\theta$$

(2.1.2)

where θ is the dip angle of the symmetry axis measured from vertical, and ϕ is the azimuth.

Using equation (2.1.1), Fletcher et al. (2009) proposed the pseudo-acoustic wave equation in TTI media and Chu et al. (2011) proposed the pure-acoustic wave equation in TTI media.

$$\frac{\partial^2 \boldsymbol{P}}{\partial t^2} = v_{px}^2 H_2 \boldsymbol{P} + \alpha v_{pz}^2 H_1 \boldsymbol{Q} + v_{sz}^2 H_1 (\boldsymbol{P} - \alpha \boldsymbol{Q}) \ ,$$

$$\frac{\partial^2 \boldsymbol{Q}}{\partial t^2} = \frac{v_{pn}^2}{\alpha} H_2 \boldsymbol{P} + v_{pz}^2 H_1 \boldsymbol{Q} - v_{sz}^2 H_2 (\frac{1}{\alpha} \boldsymbol{P} - \boldsymbol{Q})$$

(2.1.3)

$$v_{px}^2 \left(\frac{\partial^2 \boldsymbol{Q}}{\partial \hat{x}^2} + \frac{\partial^2 \boldsymbol{Q}}{\partial \hat{y}^2} \right) + v_{pz}^2 \frac{\partial^2 \boldsymbol{Q}}{\partial \hat{z}^2} = \boldsymbol{P} \ ,$$

$$\frac{\partial^2 \boldsymbol{P}}{\partial t^2} = v_{px}^2 \left(\frac{\partial^2 \boldsymbol{P}}{\partial \hat{x}^2} + \frac{\partial^2 \boldsymbol{P}}{\partial \hat{y}^2} \right) + v_{pz}^2 \frac{\partial^2 \boldsymbol{P}}{\partial \hat{z}^2} + v_{pz}^2 (v_{pn}^2 - v_{px}^2) (\frac{\partial^4 \boldsymbol{Q}}{\partial \hat{x}^2 \partial \hat{z}^2} + \frac{\partial^4 \boldsymbol{Q}}{\partial \hat{y}^2 \partial \hat{z}^2})$$

(2.1.4)

Equation (2.1.3) is the pseudo-acoustic wave equation and equation (2.1.4) is the pure-acoustic wave equation where $\boldsymbol{P}$ and $\boldsymbol{Q}$ are the wavefields; the differential operators $H_1$and H_2 in equation (2.1.3) are given by

$$\mathrm{H}_1 = \sin^2\theta \cos^2\phi \frac{\partial^2}{\partial x^2} + \sin^2\theta \sin^2\phi \frac{\partial^2}{\partial y^2} + \cos^2\theta \frac{\partial^2}{\partial z^2}$$

$$+ \sin^2\theta \, sin2\phi \frac{\partial^2}{\partial x \partial y} + sin2\theta sin\phi \frac{\partial^2}{\partial y \, \partial z} + sin2\theta cos\phi \frac{\partial^2}{\partial x \, \partial z} \ ,$$

$$\mathrm{H}_2 = \frac{\partial^2}{\partial x^2} + \frac{\partial^2}{\partial y^2} + \frac{\partial^2}{\partial z^2} - H_1$$

(2.1.5)

The differential operators $\frac{\partial^2}{\partial \hat{x}^2}$, $\frac{\partial^2}{\partial \hat{y}^2}$, and $\frac{\partial^2}{\partial \hat{z}^2}$ in equation (2.1.4) contain coordinate transformations, as follows:

$$\begin{aligned}\frac{\partial^2}{\partial \hat{x}^2} \equiv \cos^2\theta\cos^2\phi\frac{\partial^2}{\partial x^2} + \cos^2\theta\sin^2\phi\frac{\partial^2}{\partial y^2} + \sin^2\theta\frac{\partial^2}{\partial z^2} \\ + \cos^2\theta\, sin2\phi\frac{\partial^2}{\partial x\partial y} - sin2\theta cos\phi\frac{\partial^2}{\partial x\partial z} \\ - sin2\theta sin\phi\frac{\partial^2}{\partial y\partial z}\ ,\end{aligned}$$

$$\frac{\partial^2}{\partial \hat{y}^2} \equiv \sin^2\phi\frac{\partial^2}{\partial x^2} + \cos^2\phi\frac{\partial^2}{\partial y^2} - \sin^2 2\phi\frac{\partial^2}{\partial x\partial y}\ ,$$

$$\begin{aligned}\frac{\partial^2}{\partial \hat{z}^2} \equiv sin^2\theta\cos^2\phi\frac{\partial^2}{\partial x^2} + \sin^2\theta\sin^2\phi\frac{\partial^2}{\partial y^2} + \cos^2\theta\frac{\partial^2}{\partial z^2} \\ + \sin^2\theta\, sin2\phi\frac{\partial^2}{\partial x\partial y} + sin2\theta cos\phi\frac{\partial^2}{\partial x\partial z} + sin2\theta sin\phi\frac{\partial^2}{\partial y\partial z}\end{aligned}$$

(2.1.6)

The pseudo-acoustic wave equations are only valid if the condition $\epsilon \geq \delta$ is satisfied. In reality, however, rock properties may not satisfy this condition (Thomsen, 1986; Wang, 2002). Moreover, the presence of S-waves in the solution of pseudo-acoustic wave equations can cause numerical instability for TTI media that exhibit large variations in dip and azimuth symmetry angles (Fletcher et al., 2009). Moreover, wavefields computed using the pseudo-acoustic wave equations contain undesired S-wave components. When applied to RTM, these S-wave components may introduce artifacts into migration

images, and we hypothesize that these S-wave artifacts will affect the waveform inversion results.

Several approaches have been proposed to address different aspects of the aforementioned issues. To eliminate source-generated S-wave artifacts, one may surround the source with either an isotropic or elliptically anisotropic material (Alkhalifah, 2000). However, as waves propagate in the subsurface, P-waves can convert SV-waves. These converted S-waves can be suppressed by applying a filter at each time step (Zhang et al. 2009). In contrast, the pure-acoustic wave equation does not possess a stability condition for Thomsen's anisotropy parameters and completely eliminates the S-wave artifacts.

By reconstructing the pseudo-acoustic wave equation (2.1.3) and the pure-acoustic wave equation (2.1.4), we can obtain equations for two-dimensional VTI(vertical transversely isotropic) media represented by Thomsen's anisotropy parameters.

$$\frac{1}{v_{pz}^2}\frac{\partial^2 \boldsymbol{P}(x,z,t)}{\partial t^2} = (1+2\epsilon)\frac{\partial^2 \boldsymbol{P}(x,z,t)}{\partial x^2} + \frac{\partial^2 \boldsymbol{Q}(x,z,t)}{\partial z^2}$$

$$\frac{1}{v_{pz}^2}\frac{\partial^2 \boldsymbol{Q}(x,z,t)}{\partial t^2} = (1+2\delta)\frac{\partial^2 \boldsymbol{P}(x,z,t)}{\partial x^2} + \frac{\partial^2 \boldsymbol{Q}(x,z,t)}{\partial z^2}$$

(2.1.7)

$$\frac{1}{v_{pz}^2}\boldsymbol{P}(x,z,t) = (1+2\epsilon)\frac{\partial^2 \boldsymbol{Q}(x,z,t)}{\partial x^2} + \frac{\partial^2 \boldsymbol{Q}(x,z,t)}{\partial z^2}$$

$$\frac{1}{v_{pz}^2}\frac{\partial^2 \boldsymbol{P}(x,z,t)}{\partial t^2} = (1+2\epsilon)\frac{\partial^2 \boldsymbol{P}(x,z,t)}{\partial x^2} + \frac{\partial^2 \boldsymbol{P}(x,z,t)}{\partial z^2} + 2v_{pz}^2(\delta-\epsilon)\frac{\partial^4 \boldsymbol{Q}(x,z,t)}{\partial x^2 \partial z^2}$$

(2.1.8)

The pseudo-acoustic, and pure-acoustic wave equations in the frequency-domain can be obtained by taking Fourier transforms of equations (2.1.7) and (2.1.8), yielding

$$-\frac{\omega^2}{v_{pz}^2}\boldsymbol{P}(\widetilde{x,z,\omega}) = (1+2\epsilon)\frac{\partial^2 \boldsymbol{P}(\widetilde{x,z,\omega})}{\partial x^2} + \frac{\partial^2 \boldsymbol{Q}(\widetilde{x,z,\omega})}{\partial z^2}$$

$$-\frac{\omega^2}{v_{pz}^2}\boldsymbol{Q}(\widetilde{x,z,\omega}) = (1+2\delta)\frac{\partial^2 \boldsymbol{P}(\widetilde{x,z,\omega})}{\partial x^2} + \frac{\partial^2 \boldsymbol{Q}(\widetilde{x,z,\omega})}{\partial z^2}$$

(2.1.9)

$$\frac{1}{v_{pz}^2}\boldsymbol{P}(\widetilde{x,z,\omega}) = (1+2\epsilon)\frac{\partial^2 \boldsymbol{Q}(\widetilde{x,z,\omega})}{\partial x^2} + \frac{\partial^2 \boldsymbol{Q}(\widetilde{x,z,\omega})}{\partial z^2}$$

$$-\frac{w^2}{v_{pz}^2}\boldsymbol{P}(\widetilde{x,z,\omega}) = (1+2\epsilon)\frac{\partial^2 \boldsymbol{P}(\widetilde{x,z,\omega})}{\partial x^2} + \frac{\partial^2 \boldsymbol{P}(\widetilde{x,z,\omega})}{\partial z^2} + 2v_{pz}^2(\delta-\epsilon)\frac{\partial^4 \boldsymbol{Q}(\widetilde{x,z,\omega})}{\partial x^2 \partial z^2}$$

(2.1.10)

where

$$\boldsymbol{P}(\widetilde{x,z,\omega}) = \int_{-\infty}^{\infty} \boldsymbol{P}(x,z,t)e^{-i\omega t}dt\,,\quad \boldsymbol{Q}(\widetilde{x,z,\omega}) = \int_{-\infty}^{\infty} \boldsymbol{Q}(x,z,t)e^{-i\omega t}dt$$

2.2 Simulation of pseudo-acoustic and pure-acoustic wave propagation in the frequency-domain using the FEM

Pseudo-acoustic and pure-acoustic wave propagation was simulated in the domain shown in Figure 1. The symbol Ω represents the modeling domain and the symbol Ω_{pml} denotes the absorbing zone for the application of the perfectly matched layer boundary condition. The Neumann boundary condition is applied around the entire domain, $\partial\Omega$.

The pseudo-acoustic wave equation in the frequency-domain, equation (2.1.9), can be represented in the FEM formulation.

$$\int_{\Omega} -\frac{\omega^2}{v_{pz}^2}\,\widetilde{\boldsymbol{P}}\boldsymbol{\Gamma}\,d\Omega = \int_{\Omega} (1+2\epsilon)\frac{\partial^2\widetilde{\boldsymbol{P}}}{\partial x^2}\,\boldsymbol{\Gamma}\,\mathrm{d}\Omega + \int_{\Omega} \frac{\partial^2\widetilde{\boldsymbol{Q}}}{\partial z^2}\boldsymbol{\Gamma}\,d\Omega$$

$$\int_{\Omega} -\frac{\omega^2}{v_{pz}^2}\,\widetilde{\boldsymbol{Q}}\boldsymbol{\Gamma}\,d\Omega = \int_{\Omega} (1+2\delta)\frac{\partial^2\widetilde{\boldsymbol{P}}}{\partial x^2}\,\boldsymbol{\Gamma}\,\mathrm{d}\Omega + \int_{\Omega} \frac{\partial^2\widetilde{\boldsymbol{Q}}}{\partial z^2}\boldsymbol{\Gamma}\,d\Omega$$

(2.2.1)

The pure-acoustic wave equation in the frequency-domain, equation (2.1.10), can be expressed in the FEM formulation.

$$\int_{\Omega} \frac{1}{v_{pz}^2}\widetilde{\boldsymbol{P}}\boldsymbol{\Gamma}\,\mathrm{d}\Omega = \int_{\Omega} (1+2\epsilon)\frac{\partial^2\widetilde{\boldsymbol{P}}}{\partial x^2}\boldsymbol{\Gamma}\,d\Omega + \int_{\Omega} \frac{\partial^2\widetilde{\boldsymbol{Q}}}{\partial z^2}\boldsymbol{\Gamma}\,d\Omega$$

$$\int_{\Omega} -\frac{\omega^2}{v_{pz}^2}\widetilde{\boldsymbol{P}}\boldsymbol{\Gamma}\,\mathrm{d}\Omega = \int_{\Omega} (1+2\epsilon)\frac{\partial^2\widetilde{\boldsymbol{P}}}{\partial x^2}\boldsymbol{\Gamma}\,d\Omega + \int_{\Omega} \frac{\partial^2\widetilde{\boldsymbol{P}}}{\partial z^2}\boldsymbol{\Gamma}\,d\Omega$$

$$+\int_{\Omega} 2v_{pz}^{2}(\delta-\epsilon)\frac{\partial^{4}\widetilde{\boldsymbol{Q}}}{\partial x^{2}\partial z^{2}}\boldsymbol{\Gamma}\,d\Omega$$

(2.2.2)

where $\widetilde{\boldsymbol{P}}=\sum_i \alpha_i\phi_i$, $\widetilde{\boldsymbol{Q}}=\sum_i \gamma_i\phi_i$, and $\boldsymbol{\Gamma}=\sum_j \beta_j\phi_j$; $\phi_{i,j}$ is the shape function; and i and j are nodal points.

Equations (2.2.1) and (2.2.2) can be rewritten in a matrix form as follows (Marfurt. 1984):

$$\mathbf{Su}=\mathbf{f}=\begin{cases}\left(\mathbf{M_{pe}}+\mathbf{K_{pe}}\right)\mathbf{u}\\ \left(\mathbf{M_{pu}}+\mathbf{K_{pu}}+\mathbf{E}\right)\mathbf{u}\end{cases}$$

(2.2.3)

where $\mathbf{S}$ is the complex impedance matrix; $\mathbf{M_{pe}}$ and $\mathbf{M_{pu}}$ are the mass matrices; $\mathbf{K_{pe}}$ and $\mathbf{K_{pu}}$ are the stiffness matrices; $\mathbf{E}$ is a non-elliptic matrix, and it can determine wavefield propagation, such as elliptical or non-elliptical cases; $\mathbf{u}$ is the wavefield vector, and $\mathbf{f}$ is the source vector.

Equations (2.2.1) and (2.2.2) have different constructions of the impedance matrix,

$$\mathbf{u}=\begin{pmatrix}\widehat{\boldsymbol{P}}\\ \widehat{\boldsymbol{Q}}\end{pmatrix}$$

$$\mathbf{M_{pe}}=\begin{pmatrix}\boldsymbol{m_{11}} & 0\\ 0 & \boldsymbol{m_{22}}\end{pmatrix}$$

$$\mathbf{K_{pe}}=\begin{pmatrix}\boldsymbol{k_{11}} & \boldsymbol{k_{12}}\\ \boldsymbol{k_{21}} & \boldsymbol{k_{22}}\end{pmatrix}$$

$$\mathbf{f}=\begin{pmatrix}\boldsymbol{f_x}\\ \boldsymbol{f_z}\end{pmatrix}$$

(2.2.4)

$$\mathbf{u} = \begin{pmatrix} \widehat{\boldsymbol{P}} \\ \widehat{\boldsymbol{Q}} \end{pmatrix}$$

$$\mathbf{M_{pu}} = \begin{pmatrix} \boldsymbol{m_{11}} & 0 \\ \boldsymbol{m_{21}} & 0 \end{pmatrix}$$

$$\mathbf{K_{pu}} = \begin{pmatrix} \boldsymbol{k_{11}} & 0 \\ 0 & \boldsymbol{k_{22}} \end{pmatrix}$$

$$\mathbf{E} = \begin{pmatrix} 0 & \boldsymbol{e_{12}} \\ 0 & 0 \end{pmatrix}$$

$$\mathbf{f} = \begin{pmatrix} \boldsymbol{f_x} \\ \boldsymbol{f_z} \end{pmatrix}$$

(2.2.5)

where $\boldsymbol{f_x}$and $\boldsymbol{f_z}$ are the horizontal and vertical source vectors, respectively.

The components of the mass matrix and stiffness matrix for equation (2.2.4) are expressed as follows:

$$\boldsymbol{m_{11}} = \sum_{\mathrm{i}} \sum_{j} \beta_j \{ \alpha_i \int_{\Omega} -\frac{\omega^2}{v_{pz}^2} Sx_{i,j} Sz_{i,j} \phi_i \phi_j \, d\Omega \}$$

$$\boldsymbol{m_{22}} = \sum_{\mathrm{i}} \sum_{j} \beta_j \{ \gamma_i \int_{\Omega} -\frac{\omega^2}{v_{pz}^2} Sx_{i,j} Sz_{i,j} \phi_i \phi_j \, d\Omega \}$$

$$\boldsymbol{k_{11}} = \sum_{\mathrm{i}} \sum_{j} \beta_j \{ \alpha_i \int_{\Omega} (1 + 2\epsilon) \frac{Sz_{i,j}}{Sx_{i,j}} \frac{\partial \phi_i}{\partial x} \frac{\partial \phi_j}{\partial x} \, d\Omega \}$$

$$\boldsymbol{k_{21}} = \sum_{\mathrm{i}} \sum_{j} \beta_j \{ \alpha_i \int_{\Omega} (1 + 2\delta) \frac{Sz_{i,j}}{Sx_{i,j}} \frac{\partial \phi_i}{\partial x} \frac{\partial \phi_j}{\partial x} \, d\Omega \}$$

$$\boldsymbol{k_{12}} = \boldsymbol{k_{22}} = \sum_{\mathrm{i}} \sum_{j} \beta_j \{ \gamma_i \int_{\Omega} \frac{Sx_{i,j}}{Sz_{i,j}} \frac{\partial \phi_i}{\partial z} \frac{\partial \phi_j}{\partial z} \, d\Omega \}$$

(2.2.6)

Moreover, the components of the mass matrix, stiffness matrix, and non-elliptic matrix for equation (2.2.5) are expressed as follows:

$$\boldsymbol{m_{11}} = \sum_{\mathrm{i}} \sum_{j} \beta_j \{ \alpha_i \int_{\Omega} -\frac{\omega^2}{v_{pz}^2} Sx_{i,j} Sz_{i,j} \phi_i \phi_j \, d\Omega \}$$

$$\boldsymbol{m_{21}} = \sum_{\mathrm{i}} \sum_{j} \beta_j \{ \alpha_i \int_{\Omega} \frac{1}{v_{pz}^2} Sx_{i,j} Sz_{i,j} \phi_i \phi_j \, d\Omega \}$$

$$\boldsymbol{k_{11}} = \sum_{\mathrm{i}} \sum_{j} \beta_j \{ \alpha_i \int_{\Omega} (1 + 2\epsilon) \frac{Sz_{i,j}}{Sx_{i,j}} \frac{\partial \phi_i}{\partial x} \frac{\partial \phi_j}{\partial x} \, d\Omega + \alpha_i \int_{\Omega} \frac{Sx_{i,j}}{Sz_{i,j}} \frac{\partial \phi_i}{\partial z} \frac{\partial \phi_j}{\partial z} \, d\Omega \}$$

$$\boldsymbol{k_{22}} = \sum_{\mathrm{i}} \sum_{j} \beta_j \{ \gamma_i \int_{\Omega} (1 + 2\epsilon) \frac{Sz_{i,j}}{Sx_{i,j}} \frac{\partial \phi_i}{\partial x} \frac{\partial \phi_j}{\partial x} \, d\Omega + \alpha_i \int_{\Omega} \frac{Sx_{i,j}}{Sz_{i,j}} \frac{\partial \phi_i}{\partial z} \frac{\partial \phi_j}{\partial z} \, d\Omega \}$$

$$\boldsymbol{e_{12}} = \sum_{\mathrm{i}} \sum_{j} \beta_j \{ \gamma_i \int_{\Omega} -2v_{pz}^2 (\delta - \epsilon) \frac{1}{Sx_{i,j} Sz_{i,j}} \frac{\partial \phi_i}{\partial x} \frac{\partial \phi_i}{\partial z} \frac{\partial \phi_j}{\partial x} \frac{\partial \phi_j}{\partial z} \, d\Omega \}$$

(2.2.7)

$Sx_{i,j}$ and $Sz_{i,j}$ in equation (2.2.6) and (2.2.7) are the PML constants that are defined for each element. The practical definitions of the PML constants can be written as:

$$Sx_{i,j} = \begin{cases} 1 & (i,j \notin \Omega_{pml}) \\ 1 + i\xi_x/\omega & (i,j \in \Omega_{pml}) \end{cases}$$

$$\xi_x = \frac{3C_0}{2a}\log R\left(\frac{\hat{x}}{a}\right)^2$$

$$Sz_{i,j} = \begin{cases} 1 & (i,j \notin \Omega_{pml}) \\ 1 + i\xi_z/\omega & (i,j \in \Omega_{pml}) \end{cases}$$

$$\xi_z = \frac{3C_0}{2a}\log R\left(\frac{\hat{z}}{a}\right)^2$$

where a is the thickness of the boundary layer, C_0 is the velocity of the PML boundary zone, R=1000, and $\hat{x}$ and $\hat{z}$ are the distances of the x-axis and z-axis in the boundary layer (Cohen, 2002).

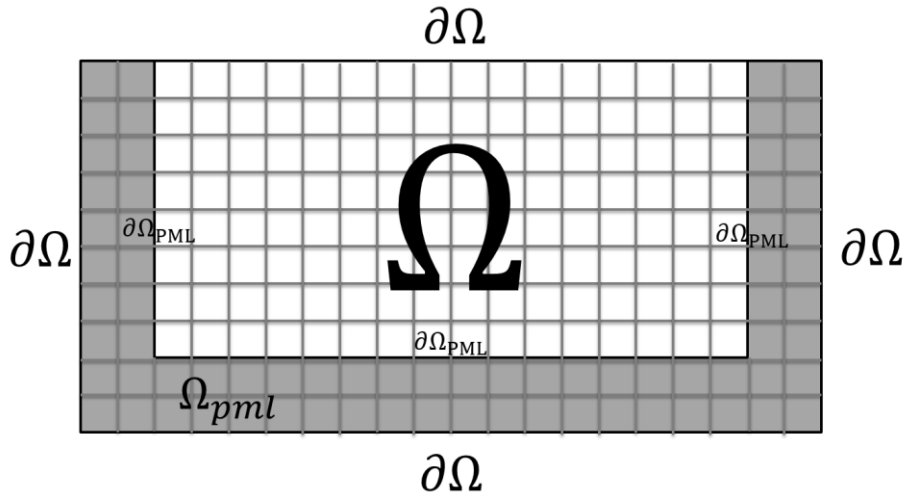

Figure 1. The pseudo-acoustic and pure-acoustic modeling domain for wave propagation. Ω is the entire domain, $\partial\Omega$ is the Neumann boundary condition, Ω_{pml} represents the absorbing boundary condition, and $\partial\Omega_{pml}$ is the boundary of the PML zone.

By solving equation (2.2.3) using the direct matrix solver, we can obtain the pseudo-acoustic and pure-acoustic wave propagation in the frequency-domain. I simulated the forward modeling in the frequency-domain and obtained the pseudo-acoustic and pure-acoustic wave propagation in the time-domain using IFT(inverse Fourier transforms)

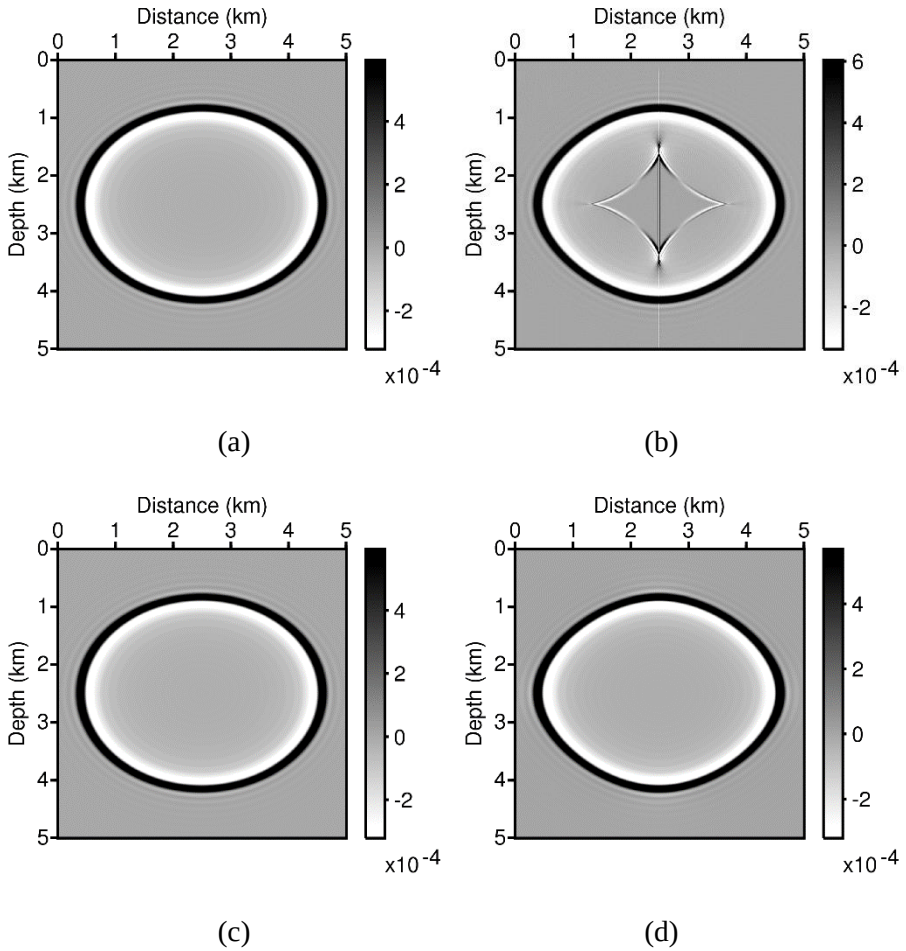

Figure 2. p-wave=2000 m/s, (a)Snapshot of pseudo-acoustic wave propagation (epsilon=0.3, delta=0.3), (b)Snapshot of pseudo-acoustic wave propagation (epsilon=0.3, delta=0.05), (c)Snapshot of pure-acoustic wave propagation (epsilon=0.3, delta=0.3), (d)Snapshot of pure-acoustic wave propagation (epsilon=0.3, delta=0.05)

In Figure 2 a and c, we can observe that the wave propagated in an elliptical

shape when ϵ and δ are equal. In Figure 2 b and d, however, the wave propagated in a non-elliptical shape when ϵ and δ are not equal. Additionally, shear-wave artifacts can be observed around the source position when using the pseudo-acoustic wave equation and the non-elliptical case.

2.3 Waveform inversion in the frequency-domain

The basic concept of waveform inversion involves reducing the residual between the observed data and modeled data using objective functions. In this study, we used the $l_2 - norm$ objective function, which is one of the most widely used objective functions. The $l_2 - norm$ objective function at an angular frequency can be expressed as:

$$E = \frac{1}{2}\sum_{i}^{n_s}\sum_{j}^{n_r}(\tilde{\boldsymbol{u}}_{i,j} - \tilde{\boldsymbol{d}}_{i,j})(\tilde{\boldsymbol{u}}_{i,j} - \tilde{\boldsymbol{d}}_{i,j})^{*}$$

(2.3.1)

where n_s is the number of shots, n_r is the number of receivers, * denotes the complex conjugate, and $\tilde{\boldsymbol{u}}_{ij}$ and $\tilde{\boldsymbol{d}}_{ij}$ are the modeled and observed data in the frequency-domain at the i^{th} shot and j^{th} receiver, respectively.

2.3.1 Calculation of gradient direction using the steepest decent method

The steepest decent method is an iterative method for minimizing the objective function using the gradient directions for the various unknown parameters.

$$\boldsymbol{m^{l+1}} = \boldsymbol{m^{l}} - \alpha^{l} \nabla_{m} \boldsymbol{E}$$

(2.3.1.1)

where $\boldsymbol{m^{l}}$ is the model parameter vector at the l^{th} iteration, $\nabla_{m}\boldsymbol{E}$ is the steepest decent gradient directions, and α is the step length for updating.

To obtain the steepest descent gradient vectors for element k, we take the partial derivative of the objective function with respect to a model parameter $\boldsymbol{m_k}$.

$$\nabla_{m_k}\boldsymbol{E} = \frac{\partial \boldsymbol{E}}{\partial m_k} = \boldsymbol{\Re}\left[\sum_{i}^{n_s}\sum_{j}^{n_r}\left(\frac{\partial \tilde{\boldsymbol{u}}_{\boldsymbol{i,j}}}{\partial \boldsymbol{m_k}}\right)^{T}\left(\tilde{\boldsymbol{r}}_{\boldsymbol{i,j}}\right)^{*}\right]$$

(2.3.1.1)

where $\boldsymbol{\Re}$ refers to the real part of a complex value, $\tilde{\boldsymbol{r}}_{\boldsymbol{i,j}}$ is the residual vector, and T is a transposed matrix.

The wave equation in the frequency-domain can be expressed as

$$\boldsymbol{S}\tilde{\boldsymbol{u}} = \boldsymbol{f}$$

(2.3.1.2)

with

$$\boldsymbol{S} = \boldsymbol{M}\omega^2 + \boldsymbol{K}$$

(2.3.1.3)

$\boldsymbol{S}$ is an impedance matrix, $\tilde{\boldsymbol{u}}$ is a vector for the Fourier-transformed modeled wavefields, $\boldsymbol{f}$ is a source vector, $\boldsymbol{M}$ is a mass matrix, $\boldsymbol{K}$ is a stiffness matrix and, ω is a complex frequency.

To efficiently calculate the partial derivative wavefields in equation (2.3.1.1), take the partial derivative of equation (2.3.1.2) with respect to model parameter $\boldsymbol{m_l}$; thus, the partial derivative wavefields can be obtained as follows:

$$\frac{\partial \tilde{\boldsymbol{u}}}{\partial \boldsymbol{m_k}} = \boldsymbol{S}^{-1}\left(-\frac{\partial \boldsymbol{S}}{\partial \boldsymbol{m_k}}\tilde{\boldsymbol{u}}\right) = \boldsymbol{S}^{-1}\,\boldsymbol{v_k}$$

(2.3.1.4)

where $\boldsymbol{v_k}$ is a virtual source vector with respect to parameter $\boldsymbol{m_k}$. By substituting equation (2.3.1.4) into equation (2.3.1.1), the steepest decent gradient direction of a model parameter for element k can be calculated using the back propagation algorithm, and it can be expressed as

$$\nabla_{m_k}\boldsymbol{E} = \Re\left[\sum_{i}^{n_s}(\boldsymbol{v_k})^T\,(\boldsymbol{S}^{-1})^T\left(\tilde{\boldsymbol{r}}_{\boldsymbol{i}}\right)^*\right]$$

(2.3.1.5)

2.3.2 Scaling of the gradient direction using a pseudo-Hessian matrix

Computing the gradient direction using the steepest descent method requires a precondition because it is not considered the geometrical spreading effect. Pratt et al. suggested using the Gauss-Newton method and the full-Newton method for regularizing the gradient direction in 1998. However, the Gauss-Newton and the full-Newton methods require substantial computing memory and costs due to calculation of the Jacobian and Hessian matrices. The full Hessian matrix and approximate Hessian matrix can be expressed as:

$$\mathbf{H} = \mathbf{H_a} + \boldsymbol{R}$$

(2.3.2.1)

where $\mathbf{H}$ is the full Hessian matrix and $\mathbf{H_a}$ is the approximate Hessian matrix, which can be expressed as:

$$\mathbf{H_a} = \mathfrak{R}[\boldsymbol{J}^T\boldsymbol{J}^*] = \mathfrak{R}\left[\left(\frac{\partial\tilde{\boldsymbol{u}}}{\partial m_1}\ \frac{\partial\tilde{\boldsymbol{u}}}{\partial m_2}\ \cdots \frac{\partial\tilde{\boldsymbol{u}}}{\partial m_n}\right)^T \left\{\left(\frac{\partial\tilde{\boldsymbol{u}}}{\partial m_1}\right)^* \left(\frac{\partial\tilde{\boldsymbol{u}}}{\partial m_2}\right)^* \cdots \left(\frac{\partial\tilde{\boldsymbol{u}}}{\partial m_n}\right)^*\right\}\right]$$

(2.3.2.2)

where $\boldsymbol{J}$ is the Jacobian matrix. The second term of equation (2.3.2.1) corrects the Hessian for double-scattering effects in non-linear inverse problems. It can be expressed as:

$$\boldsymbol{R} = \mathfrak{R}\left[\left(\frac{\partial}{\partial m_1}\boldsymbol{J}^T\right)\tilde{\boldsymbol{r}}^* \quad \left(\frac{\partial}{\partial m_2}\boldsymbol{J}^T\right)\tilde{\boldsymbol{r}}^* \cdots \left(\frac{\partial}{\partial m_n}\boldsymbol{J}^T\right)\tilde{\boldsymbol{r}}^*\right]$$

(2.3.2.3)

In 2001, Shin et al. introduced the pseudo-Hessian matrix, which uses only the diagonal component of the approximate Hessian matrix. The pseudo-Hessian matrix has more computational efficiency than the approximate Hessian matrix. The diagonal of the approximate Hessian matrix, the so-called pseudo-Hessian matrix, is expressed as:

$$diag(\mathbf{H_a}) = \mathfrak{R}\left[\left(\frac{\partial \tilde{\boldsymbol{u}}}{\partial m_1}\right)^T \left(\frac{\partial \tilde{\boldsymbol{u}}}{\partial m_1}\right)^* \quad \left(\frac{\partial \tilde{\boldsymbol{u}}}{\partial m_2}\right)^T \left(\frac{\partial \tilde{\boldsymbol{u}}}{\partial m_2}\right)^* \cdots \left(\frac{\partial \tilde{\boldsymbol{u}}}{\partial m_n}\right)^T \left(\frac{\partial \tilde{\boldsymbol{u}}}{\partial m_n}\right)^*\right]$$

(2.3.2.4)

An element of equation (2.3.2.4) can be rewritten using equation (2.3.1.4) as:

$$\left(\frac{\partial \tilde{\boldsymbol{u}}}{\partial m_k}\right)^T \left(\frac{\partial \tilde{\boldsymbol{u}}}{\partial m_k}\right)^* = \boldsymbol{v_k^T}(\boldsymbol{S^{-1}})^T(\boldsymbol{S^{-1}})^*\boldsymbol{v_k^*}$$

(2.3.2.5)

In equation (2.3.2.5), $(\boldsymbol{S^{-1}})^T(\boldsymbol{S^{-1}})^*$ can be expressed using the impulse response and it is diagonally dominant. Therefore, we can approximate $(\boldsymbol{S^{-1}})^T(\boldsymbol{S^{-1}})^* = \mathbf{I}$, where $\mathbf{I}$ is the unit matrix. Finally the pseudo-Hessian matrix is given by:

$$\mathbf{H_p} = diag(\mathbf{H_a}) = \mathfrak{R}\left[\boldsymbol{v_k^T v_k^*}\right]$$

(2.3.2.6)

Now, equation (2.3.1.1) for a single frequency can be rewritten as:

$$\boldsymbol{m^{l+1}} = \boldsymbol{m^l} - \alpha^l \boldsymbol{NRM}\left[\frac{\sum_i^{n_s} \boldsymbol{v_k^T}(\boldsymbol{S^{-1}})^T\left(\tilde{\boldsymbol{r}}_i\right)^*}{\mathfrak{R}\left[\sum_i^{n_s} \boldsymbol{v_k^T v_k^*}\right] + \lambda \mathbf{I}}\right]$$

where $\boldsymbol{m^l}$ is the model parameter at l^{th} iteration, λ is the stabilizing constant (Marquardt, 1963), and $\boldsymbol{NRM}$ is the normalization operator.

2.3.3 Source-estimation algorithm

The source wavelet is an important factor for successful seismic waveform inversion. Because the source wavelet is unknown in observed data, we need to estimate the source wavelet during the waveform inversion process.

To derive a source estimation algorithm, the frequency-domain wave equation is expressed as:

$$\boldsymbol{Su} = \boldsymbol{F} = (e + if)$$

(2.3.4.1)

where e is the real part of the source wavelet and f is the imaginary part. Expressing the modeled wavefield in the same manner as the source wavelet yields

$$\boldsymbol{u_{ij}} = (c_i + id_i)(e + if) = (c_i e - d_i f) + i(c_i f + d_i e)$$

(2.3.4.2)

where $c_i + id_i = G_{\mathrm{i}}$ is the numerical Green's function. Additionally, the observed wavefield is expressed as $d_i = a_i + ib_i$. Then, the objective function for the source wavelet is written as:

$$\boldsymbol{E_{src}} = \frac{1}{2}\sum_{i}^{n_s}\{(c_i e - d_i f - a_i)^2 + (c_i f + d_i e - b_i)^2\}$$

(2.3.4.3)

Using a Taylor series expansion, we can write:

$$E_{src}(p + \Delta p) = E(p) + \Delta P^t \nabla \boldsymbol{E_{src}} + \frac{1}{2}\Delta p^t \boldsymbol{H_{src}} \Delta p + O^3(\Delta p)$$

(2.3.4.4)

where $= [e \quad f]^t$, $\Delta p = [\Delta e \quad \Delta f]^t$, $\nabla \boldsymbol{E_{src}}$ is the gradient, and $\boldsymbol{H_{src}}$ is the Hessian. To obtain the Δp that minimizes the objective function E_{src}, we apply the condition $\frac{\partial E_{src}}{\partial \Delta e} = 0$ and $\frac{\partial E_{src}}{\partial \Delta f} = 0$ to equation (2.3.4.3), which yields:

$$\Delta p = -\boldsymbol{H_{src}^{-1}} \nabla \boldsymbol{E_{src}}$$

(2.3.4.5)

The gradient $\nabla \boldsymbol{E_{src}}$ and the Hessian $\boldsymbol{H_{src}}$ are as follows:

$$\nabla \boldsymbol{E_{src}} = \begin{pmatrix} \frac{\partial \boldsymbol{E_{src}}}{\partial e} \\ \frac{\partial \boldsymbol{E_{src}}}{\partial f} \end{pmatrix} = \begin{pmatrix} \sum_i^{n_s} \left[\left(c_i^2 + d_i^2 \right) e - a_i c_i - b_i d_i \right] \\ \sum_i^{n_s} \left[\left(c_i^2 + d_i^2 \right) f + a_i d_i - b_i c_i \right] \end{pmatrix}$$

(2.3.4.6)

$$\boldsymbol{H_{src}} = \begin{pmatrix} \frac{\partial^2 \boldsymbol{E_{src}}}{\partial e^2} & \frac{\partial^2 \boldsymbol{E_{src}}}{\partial e \partial f} \\ \frac{\partial^2 \boldsymbol{E_{src}}}{\partial e \partial f} & \frac{\partial^2 \boldsymbol{E_{src}}}{\partial f^2} \end{pmatrix} = \begin{pmatrix} \sum_i^{n_s} c_i^2 + d_i^2 & 0 \\ 0 & \sum_i^{n_s} c_i^2 + d_i^2 \end{pmatrix}$$

(2.3.4.7)

Substituting equations (2.3.4.6) and (2.3.4.7) into equation (2.3.4.5) yields:

$$\Delta p = -\begin{pmatrix} \frac{\sum_i^{n_s} \left(c_i^2 + d_i^2 \right) e - a_i c_i - b_i d_i}{\sum_i^{n_s} c_i^2 + d_i^2} \\ \frac{\sum_i^{n_s} \left(c_i^2 + d_i^2 \right) e + a_i d_i - b_i c_i}{\sum_i^{n_s} c_i^2 + d_i^2} \end{pmatrix}$$

Accordingly, the source wavelet can be inverted by the formula

$$\boldsymbol{p} = \begin{pmatrix} \frac{\sum_i^{n_s} -a_i c_i - b_i d_i}{\sum_i^{n_s} c_i^2 + d_i^2} \\ \frac{\sum_i^{n_s} a_i d_i - b_i c_i}{\sum_i^{n_s} c_i^2 + d_i^2} \end{pmatrix} = \frac{\sum_i^{n_s} (a_i + i b_i)(c_i + i d_i)^*}{\sum_i^{n_s} (c_i + i d_i)(c_i + i d_i)^*} = \frac{\sum_i^{n_s} \boldsymbol{d_i} \boldsymbol{u_i^*}}{\sum_i^{n_s} \boldsymbol{u_i} \boldsymbol{u_i^*}}$$

where $\boldsymbol{d_i}$ is the observed data at the i^{th} shot, $\boldsymbol{u_i}$ is the modeled data at the i^{th} shot, and $*$ denotes complex conjugate.

Chapter 3 Numerical Examples

3.1 The radiation patterns of parameters.

The most important consideration in the multiparameter waveform inversion is the radiation patterns of the model parameters (Gholami et al., 2013). Multiparameter waveform inversion needs to consider the trade-off effect that occurs through mutually modeled parameters. The trade-off, which is called crosstalk is a phenomenon caused by the overlap of each parameter's radiation pattern. In scaling the Hessian matrix stage, the Hessian matrix will be distorted by the trade-off effect, and these results lead to a wrong gradient direction and could lead to the local minima. Consequently, the waveform inversion results are contaminated by undesired signals and it is difficult to obtain the desired model parameters.

The partial derivative wavefields can be easily obtained using the virtual source. To illustrate the partial derivative wavefields with respect to each model parameter, we compute the following equation:

$$\frac{\partial u}{\partial m} = \boldsymbol{S}^{-1}\boldsymbol{v}_{\boldsymbol{k}_{\boldsymbol{m}}}$$

(3.1.1)

where $\boldsymbol{v}_{\boldsymbol{k}_{\boldsymbol{m}}}$ is the virtual source vector with respect to model parameter m. We consider three cases. The first case is a homogeneous isotropic background model defined by P-wave = 3000m/s, epsilon = 0.0, and delta = 0.0. The second case is an elliptical VTI background model defined by P-wave = 3000m/s,

epsilon = 0.2, and delta = 0.2. Finally, the third case is a non-elliptical VTI background model defined by P-wave = 3000m/s, epsilon = 0.2, and delta = 0.1. The peak frequency of the source wavelet is 20 Hz. Additionally, we simulated scattering patterns with various source positions which are changed by the angle between the source and recording position: 0 degrees, 45 degrees, and 90 degrees. The virtual source is located in the midpoint of the domain. In the second case, we assumed that the background models are elliptical VTI media, which means that the values of epsilon and delta are identical. The reason why we assumed elliptical media is that the pseudo-acoustic wave equation creates shear-wave artifacts when the values of epsilon and delta are different. In general, the amplitudes of the generated shear-wave artifacts are larger than the amplitudes of the desired wavefield. Therefore, we cannot detect the scattering motion of the wavefield exactly.

0 degrees

45 degrees

90 degrees

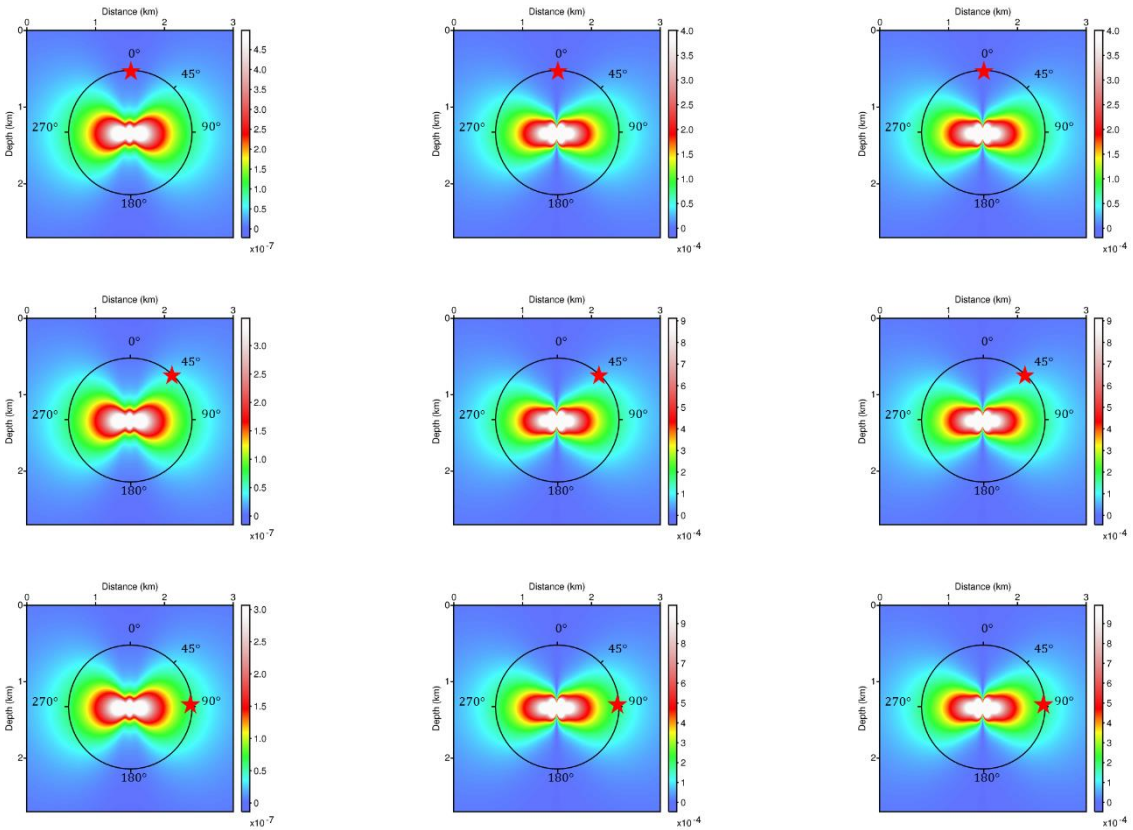

Figure 3. The radiation patterns of the pseudo-acoustic wave in isotropic media; 1st column: P-wave, 2nd column: epsilon, and 3rd column: delta

0 degrees

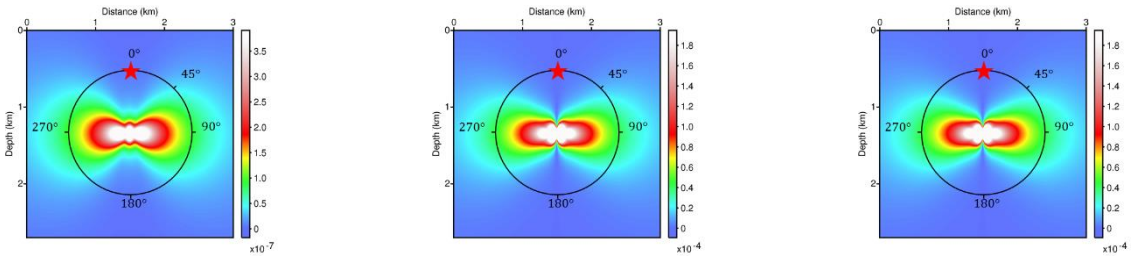

45 degrees

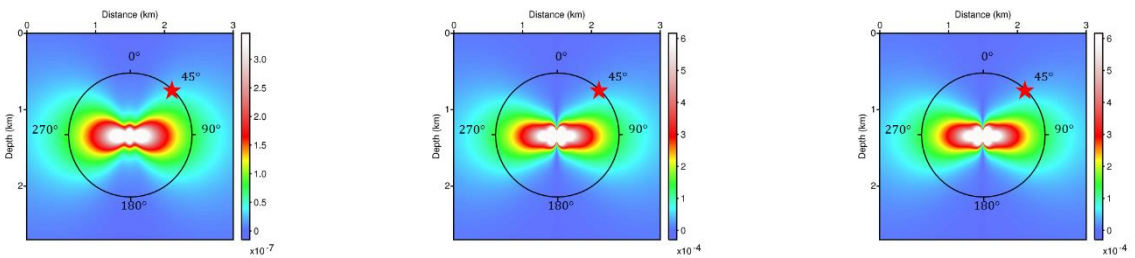

90 degrees

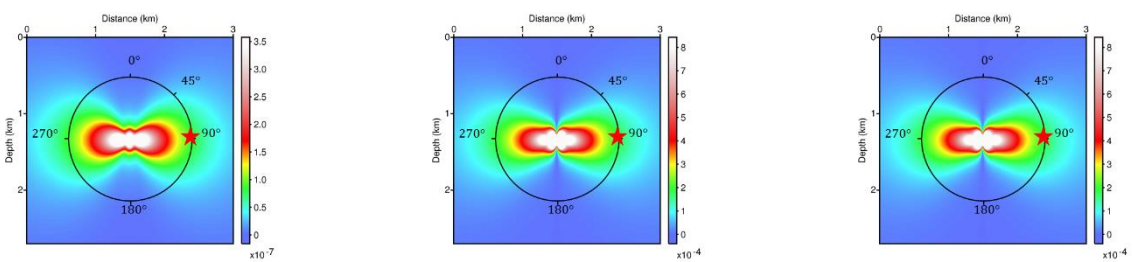

Figure 4. The radiation patterns of the pseudo-acoustic wave in elliptical VTI media; 1st column: P-wave, 2nd column: epsilon, and 3rd column: delta

0 degrees

45 degrees

90 degrees

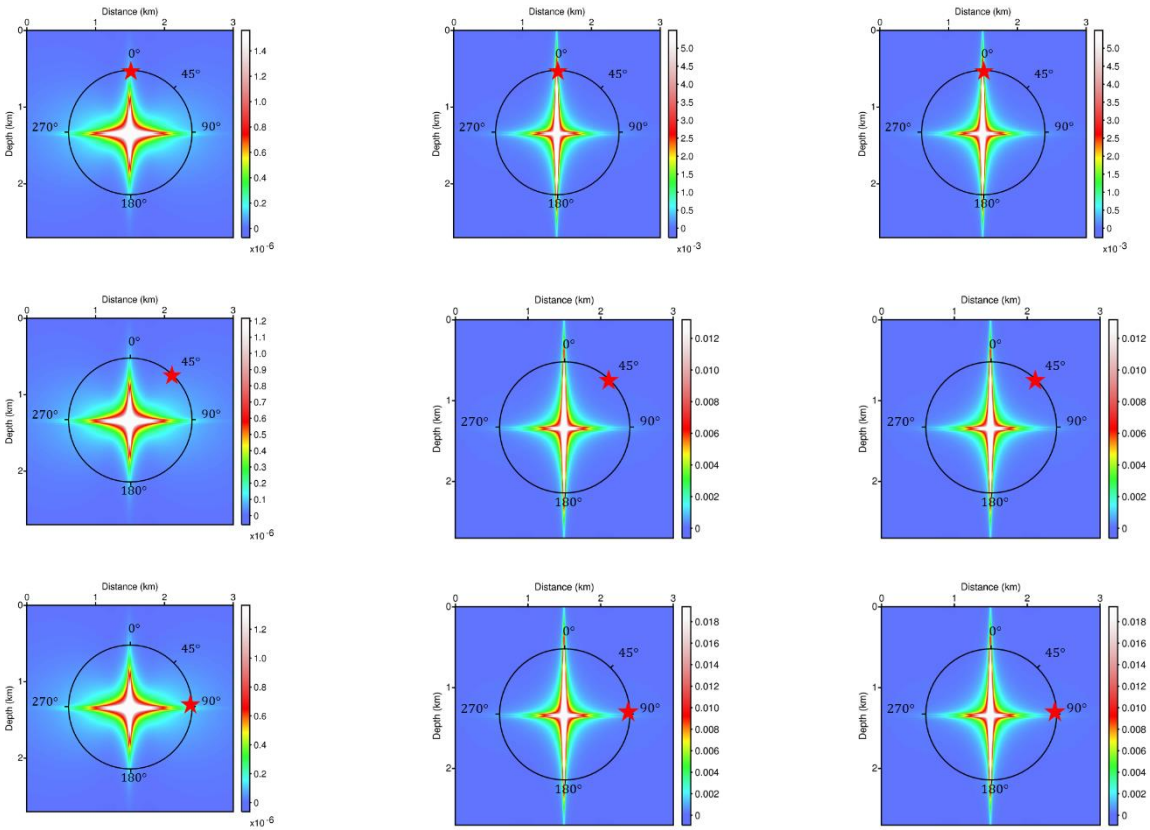

Figure 5. The radiation patterns of the pseudo-acoustic wave in non-elliptical VTI media; 1st column: P-wave, 2nd column: epsilon, and 3rd column: delta

0 degrees

45 degrees

90 degrees

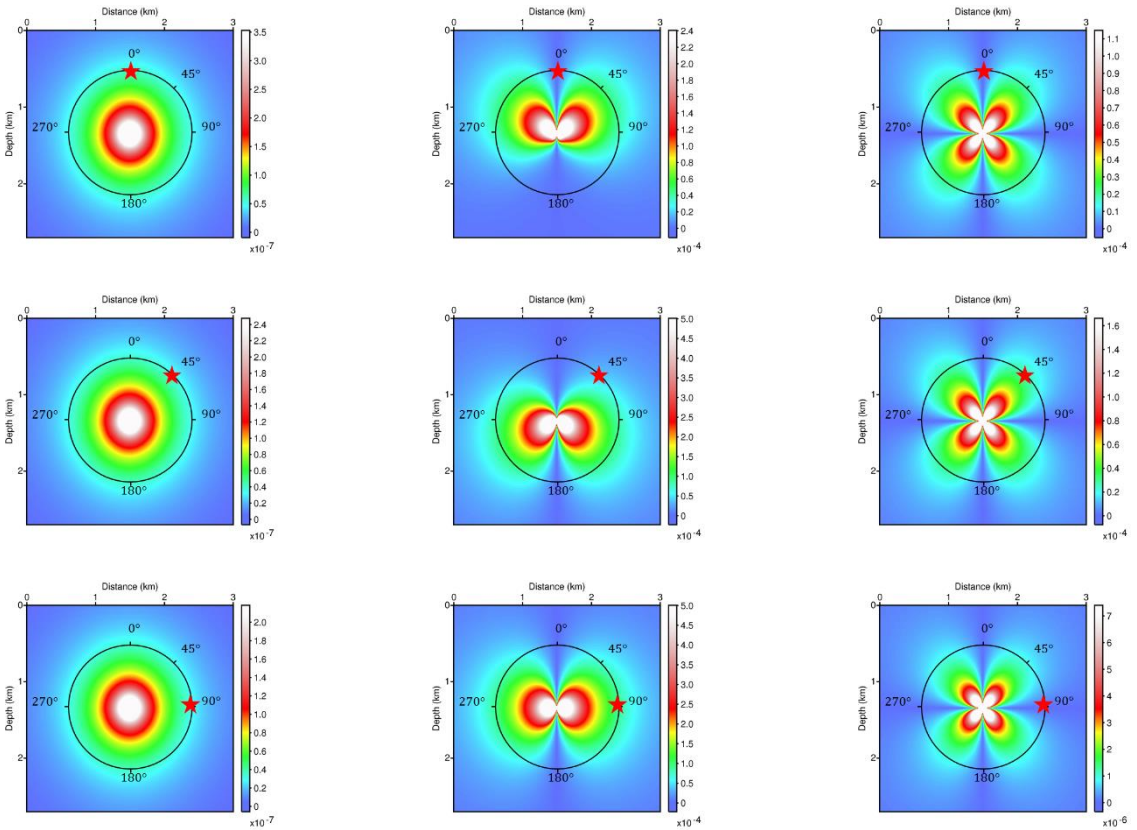

Figure 6. The radiation patterns of the pure-acoustic wave in isotropy media; 1st column: P-wave, 2nd column: epsilon, and 3rd column: delta

0 degrees

45 degrees

90 degrees

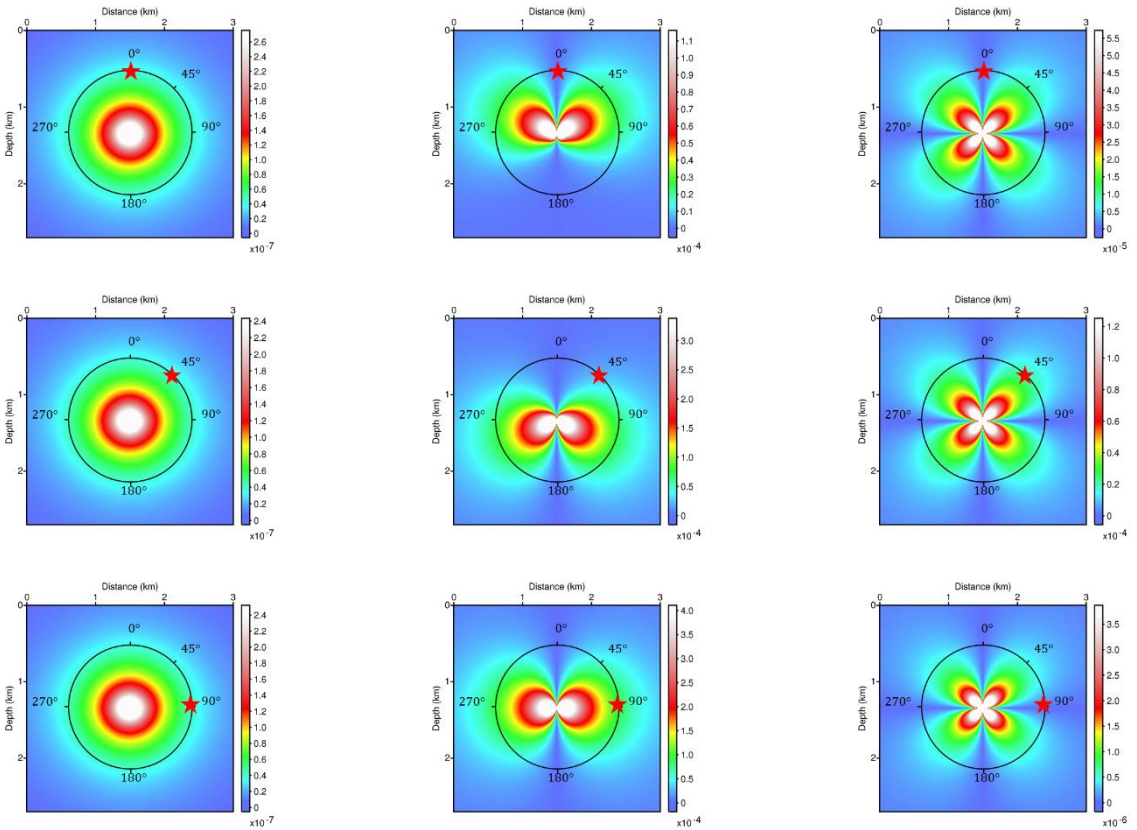

Figure 7. The radiation patterns of the pure-acoustic wave in elliptical VTI media; 1st column: P-wave, 2nd column: epsilon, and 3rd column: delta

0 degrees

45 degrees

90 degrees

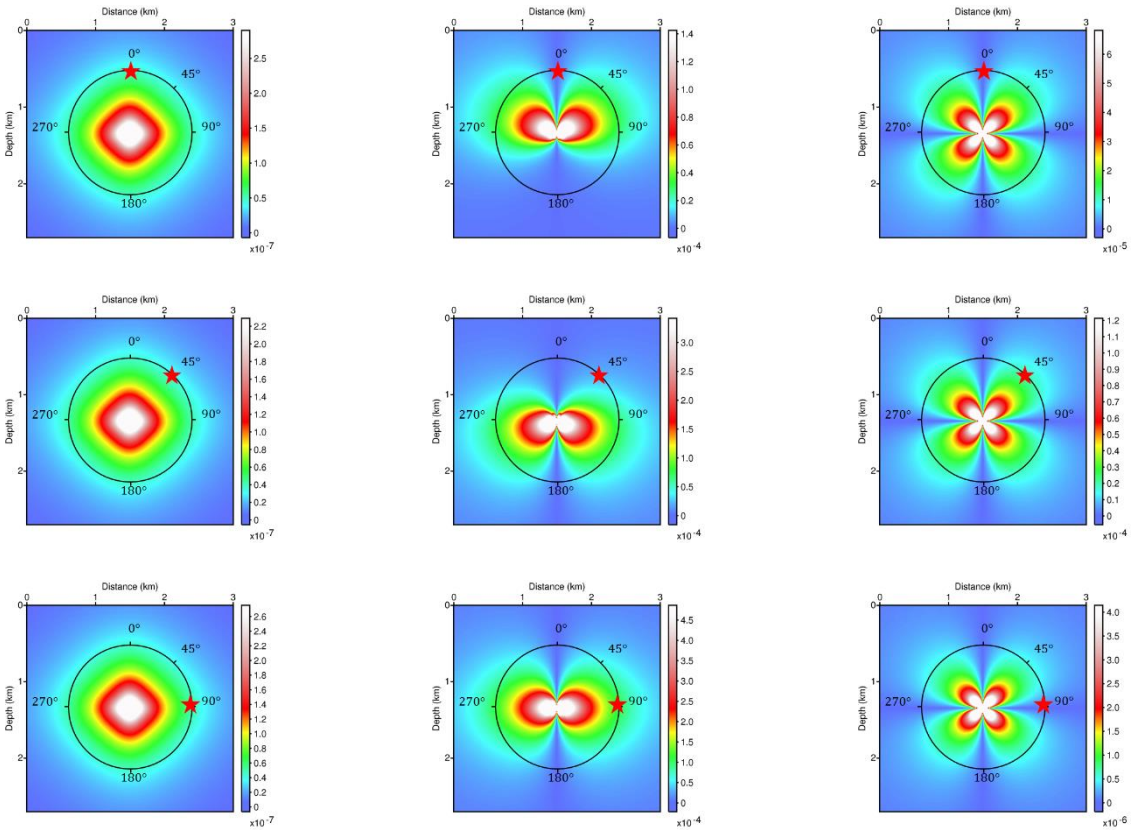

Figure 8. The radiation patterns of the pure-acoustic wave in non-elliptical VTI media; 1st column: P-wave, 2nd column: epsilon, and 3rd column: delta

According to the simulations, the radiation patterns of the pseudo-acoustic wave show similar motion for all media. Additionally, they exhibit similar scattering motion for the three cases of incidence angles. In Figure 3 and Figure 4, the spreading pattern of the P-wave and anisotropy parameters has a slightly different shape in the central part of the amplitude. In Figure 5, however, the pseudo-acoustic wave in non-elliptical VTI media generates shear-wave artifacts. Because of the generated shear-wave artifacts, we could not detect the desired wavefield motion. However, based on the results of the previous two experiments, we could predict that the wavefield in non-elliptical VTI media will exhibit similar motion as the previous two experiments. On the other hand, the radiation patterns of the pure-acoustic wave and Pseudo-Acoustic wave are significantly different. In particular, the radiation pattern of the epsilon of the pure-acoustic wave exhibited a sensitivity to the incidence angles. Conversely, the radiation patterns of the P-wave and the delta of the pure-acoustic wave were not sensitive to the incidence angles. The P-wave exhibits various spreading motions depending on the values of the anisotropy parameters.

Through these experiments, we expected that using the pure-acoustic wave for FWI is more stable than using the pseudo-acoustic wave. The reasons are as follows. First, the pure-acoustic wave would not generate shear-wave artifacts in non-elliptical VTI media. Second, the radiation pattern of the dominant parameter (P-wave) of the pure-acoustic wave spread equally in all directions because, in the multi-parameter FWI, it is important to scatter the dominant parameter in all directions (Operto et al., 2014). Third, for the pure-acoustic wave, the radiation patterns of the dominant parameter and anisotropy parameters did not considerably overlap.

3.2 Waveform inversion algorithm tests using the same forward modeling

In this section, we performed numerical tests to verify the two proposed FWI algorithms, which use the pseudo-acoustic and pure-acoustic wave equations. We generated synthetic data (observed data) using the same modeling algorithm and scheme. In other words, the synthetic data were generated using the same pseudo-acoustic wave equation and modeling scheme to test the waveform inversion algorithm with the pseudo-acoustic wave equation in the frequency-domain. The FWI algorithm using the pure-acoustic wave equation was tested in the same manner.

We used HESS VTI model parameters, which are illustrated in Figure 9. The features of the HESS VTI model include a high velocity area, which is called salt, and a fault located in the right-side of the model. Before the experiment, we assumed an elliptical case, which means that delta and epsilon have the same values at all nodal points, because the pseudo-acoustic wave equation has a modeling stability condition such as $\epsilon \geq \delta$. The values of delta and epsilon were updated by the same gradient direction derived from the epsilon parameter. We generated synthetic data in the frequency-domain from 0.01 Hz to 15.01 Hz with a step of 0.25 Hz.

We applied a smoothed P-wave velocity model and a smoothed epsilon model as the initial models, and these models were updated simultaneously. Moreover, for quality control of the waveform inversion models, we computed the relative percentage errors for the model parameters using the following equation:

$$\mathrm{err_m} = 100\frac{\sum_i^{N_x \cdot N_z} \left| \boldsymbol{m}_{cal,i} - \boldsymbol{m}_{true,i} \right|}{\sum_i^{N_x \cdot N_z} \boldsymbol{m}_{true,i}}$$

(3.2.1)

where $\boldsymbol{m}_{cal}$ and $\boldsymbol{m}_{true}$ denote the inverted model and the true model, respectively, and N_x and N_z correspond to the number of nodes in the x and z directions along a Cartesian grid.

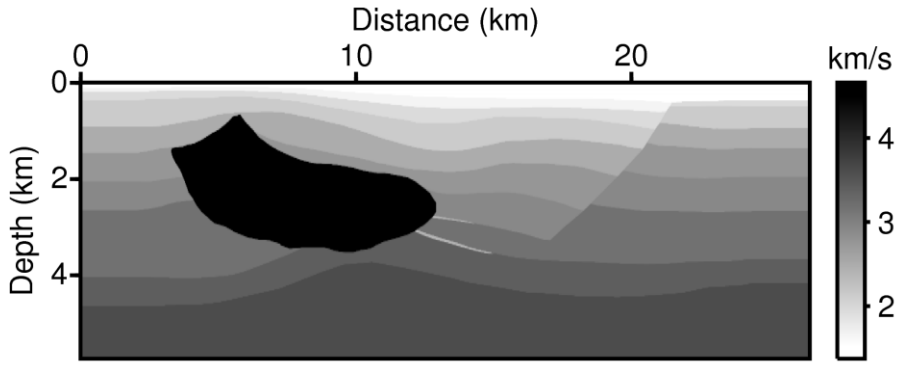

(a)

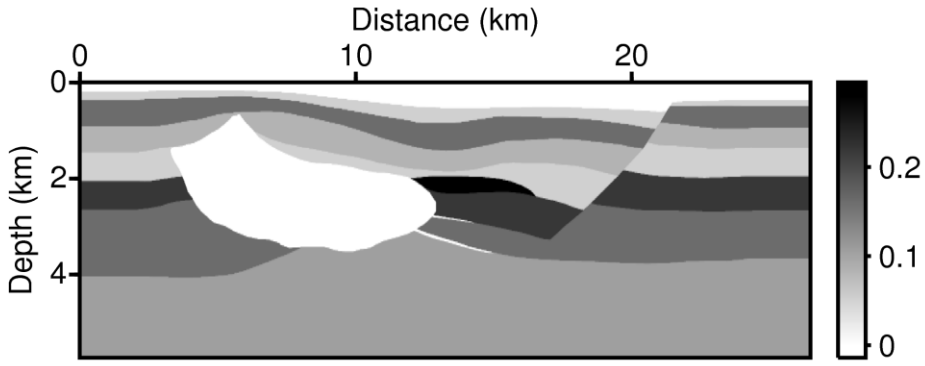

(b)

Figure 9. HESS VTI model parameter set: (a) P-wave velocity and (b) epsilon model

Summary of the information of the synthetic data	
Domain size	25,000m × 5,000m
Domain grid interval	25m
Number of shots	1000
Number of receivers	1000
Modeling scheme	Linear element FEM
Source wavelet	Impulse function

Table 1. Summary of the information of the generated frequency-domain synthetic dataset using the HESS VTI parameter set.

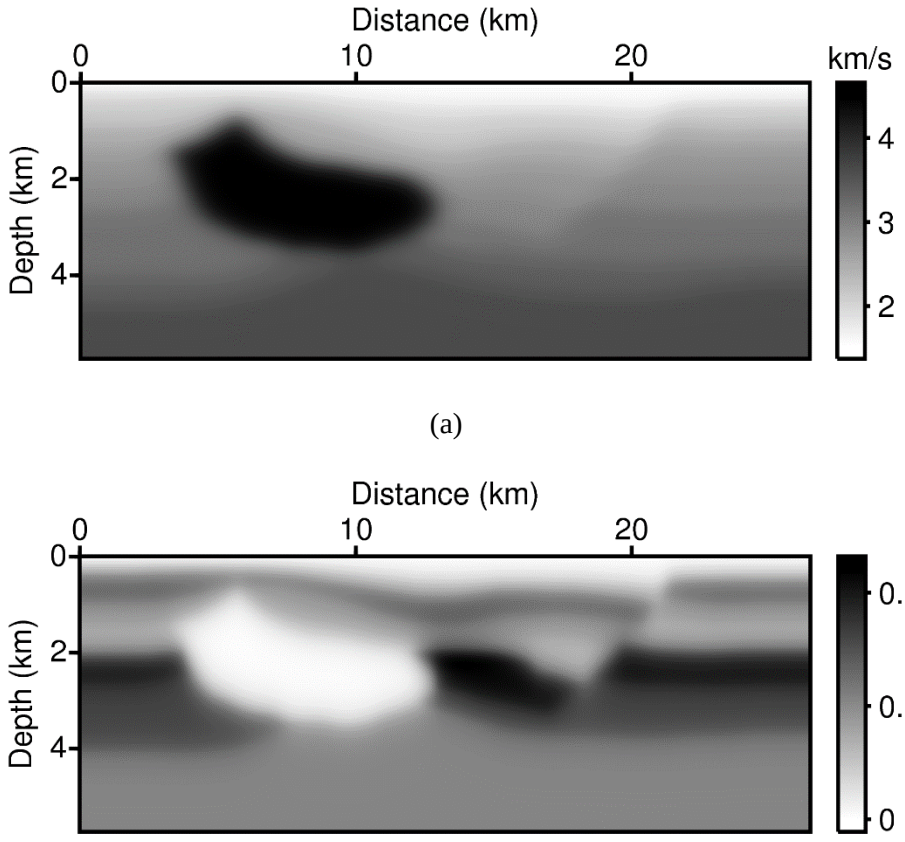

Figure 10. Initial (a) P-wave velocity and (b) epsilon model

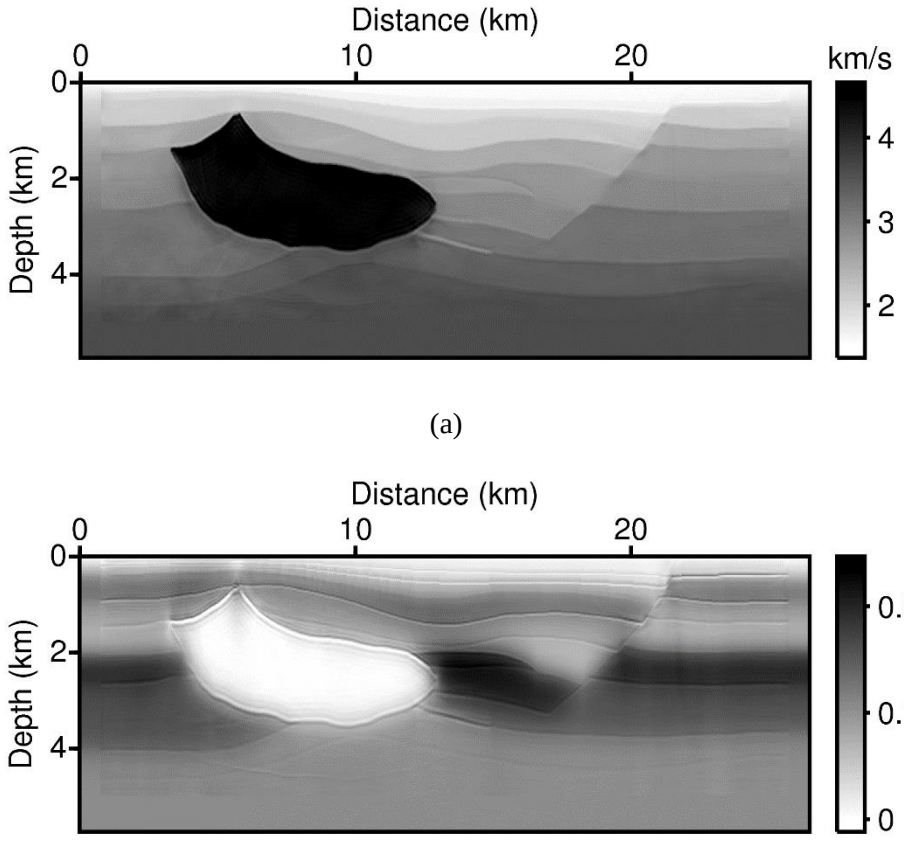

Figure 11. Inverted (a) P-wave velocity and (b) epsilon using the pseudo-acoustic wave equation algorithm

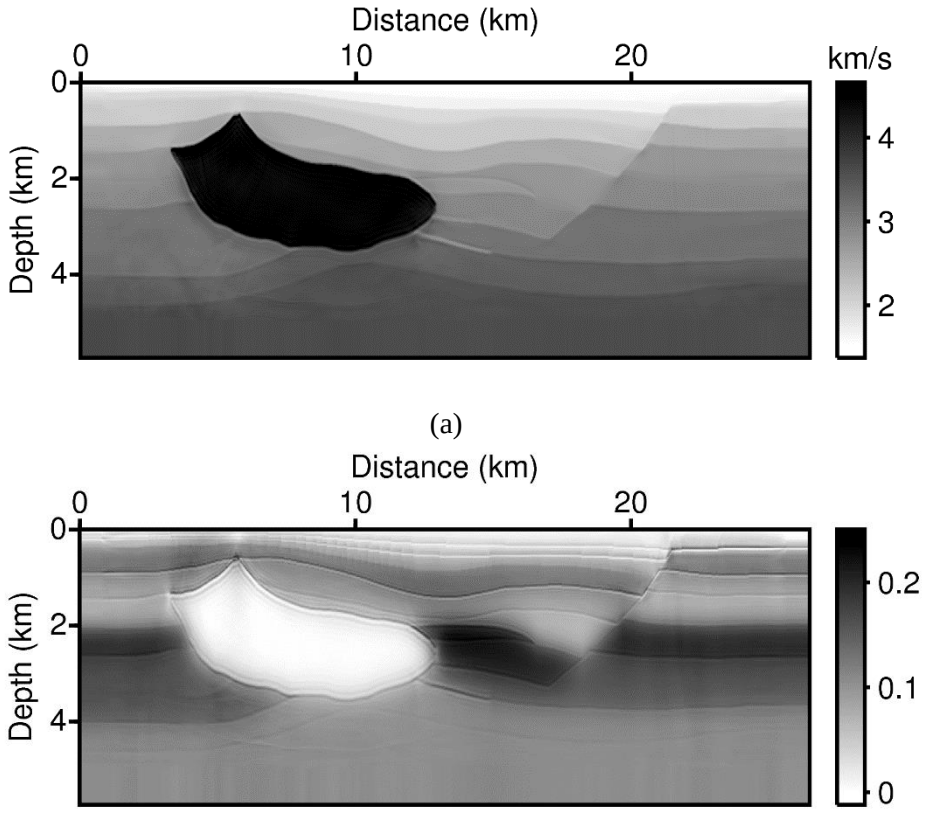

(a)

(b)

Figure 12. Inverted (a) P-wave velocity and (b) epsilon using the pure-acoustic wave equation algorithm

	Pseudo-acoustic	Pure-acoustic
Initial P-wave velocity	2.69953 %	2.69953 %
Initial Epsilon model	18.03448 %	18.03448 %
Inverted P-wave velocity	1.19012 %	1.17305 %
Inverted Epsilon model	17.75597 %	18.33332 %

Table 2. The relative percentage errors for the model parameter

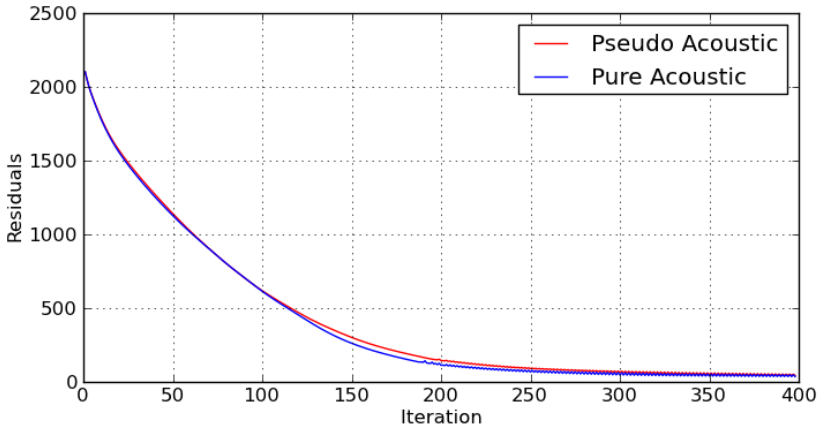

Figure 13. The residuals of both algorithms represented by the values of errors and iteration numbers.

Through the experiments, both algorithms were able to confirm that both the P-wave velocity model and the epsilon model were close to perfection. Both of the algorithms well restored specific layers, even under the high-velocity zone called the sub-salt region. As shown in the Figure 11.a and Figure 12.a, however, some artifacts occurred on the right-side of the high-velocity region of the inverted P-wave velocity model. These artifacts might be a result of the trade-off effect. Table 2 shows that the relative percentage of model misfits decreased.

The percentage error of the epsilon model calculated using the pseudo-acoustic wave equation only decreased by 0.3%, and the percentage error of the epsilon model calculated using the pure-acoustic wave equation increased by 0.3%; however, the residuals of the pure-acoustic wave equation linearly decreased. According to these results, the P-wave velocity parameter has a great influence on the waveform inversion process than does the epsilon parameter, and it is also considered that the dominant parameter is a more critical factor than the other parameters.

3.3 Time-domain synthetic data tests

In the previous chapter, we confirmed the availability and possibility of both of the proposed algorithms through numerical tests using the same modeling scheme. In this chapter, to simulate more realistic tests, we generated synthetic data in the time-domain and verified the FWI algorithms and analyzed the performance of both algorithms. We generated synthetic datasets using the Overthrust VTI model. The model parameters are illustrated in Figure 14 and details of the generated synthetic data are presented in Table 4.

We employed the elastic wave equation using the staggered-grid FDM numerical modeling scheme. We considered that the experiments are a marine environment, and we modified the original model parameters by adding the sea-water layer on the top of the model's surfaces because of the acoustic approximation of both algorithms. The addition of the sea-water layer was able to reduce the effects of the surface waves caused by the elastic wave propagation. Removal of the other elastic effects or other preprocessing was not applied. To compare both algorithms, we used 6 cases of combinations of the initial model and updating strategies.

Case	Initial P-wave velocity model	Initial epsilon model	Initial delta model
1	Smoothed P-wave velocity model	Smoothed epsilon model	Smoothed epsilon model
2	Smoothed P-wave velocity model	True epsilon model	True epsilon model
3	True P-wave velocity model	Smoothed epsilon model	Smoothed epsilon model
4	Smoothed P-wave velocity model	Smoothed epsilon model	Zero
5	Smoothed P-wave velocity model	True epsilon model	Zero
6	True P-wave velocity model	Smoothed epsilon model	Zero

Table 3. Combination of initial model parameters for comparison tests

The objective of case1 in Table 3 is to simultaneously find the P-wave velocity and epsilon, the objective of case2 is to calculate the P-wave velocity more accurately when we know the exact value of epsilon, and the objective of case3 is to calculate the value of epsilon more accurately when we know the exact value of the P-wave velocity. The objectives of cases 4 to 6 were the same as those of cases 1 to 3, but these cases completely ignored the delta value. The reason why the value of the delta parameter was set to zero is that the pseudo-acoustic wave equation has the modeling stability constraint $\epsilon \geq \delta$. In cases 4 to 6, the pseudo-acoustic wave would generate shear-wave artifacts on nodal points that have different values of epsilon and delta. Therefore, the results of cases 4 to 6 are expected to provide a good comparison of the two algorithms. The delta and epsilon would be updated by the same gradient direction derived by the epsilon parameter in cases 1 to 3, but the delta would not be updated in cases 4 to 6. The P-wave velocity and epsilon model were updated every iteration with a different step length.

Moreoever, we tested the generated synthetic datasets using the conventional isotropy waveform inversion algorithms and we compared the relative percentage of P-wave velocity model misfits for the isotropy waveform inversion algorithm and the suggested anisotropy waveform inversion algorithms.

We only inverted the P-wave velocity and epsilon parameters because of the modeling stability condition of the pseudo-acoustic wave equation and because the computing environment of our lab for solving the impedance matrix thatt considered the delta parameter would require considerable computational costs.

3.3.1 OVERTHRUST VTI Model

Unlike the frequency-domain synthetic dataset prior to the validation phase, the time-domain synthetic dataset was made similar to the realistic situation considering the value of delta. We tested the Overthrust VTI model, which contains complex fault structures. Figure 14 shows the Overthrust VTI model parameters, and Table 4 describes simple information of the dataset.

For an accurate comparison, the two algorithms were equally applicable to the initial model of the 6 cases, and we also used the same frequency group for frequency-domain FWI for both algorithms. The initial models are smoothed models, and they are illustrated in Figure 15; the components of the frequency group are from 2.625 Hz to 15.0 Hz with a 0.125 Hz interval.

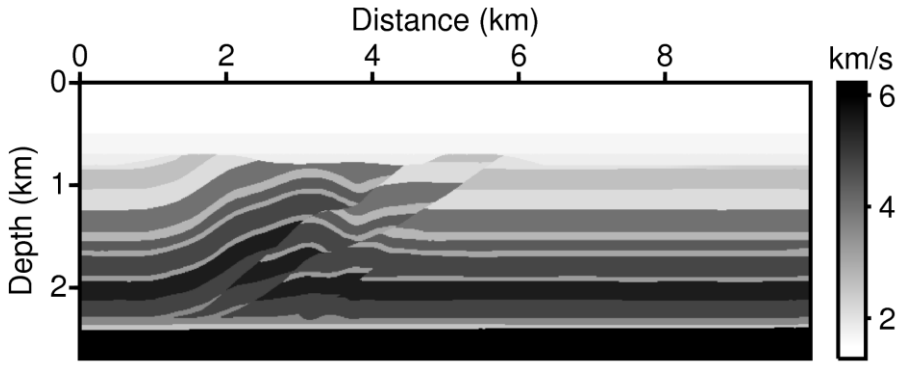

(a)

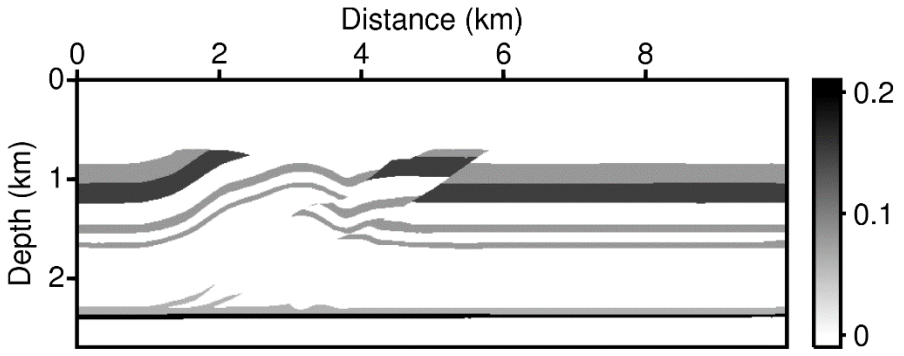

(b)

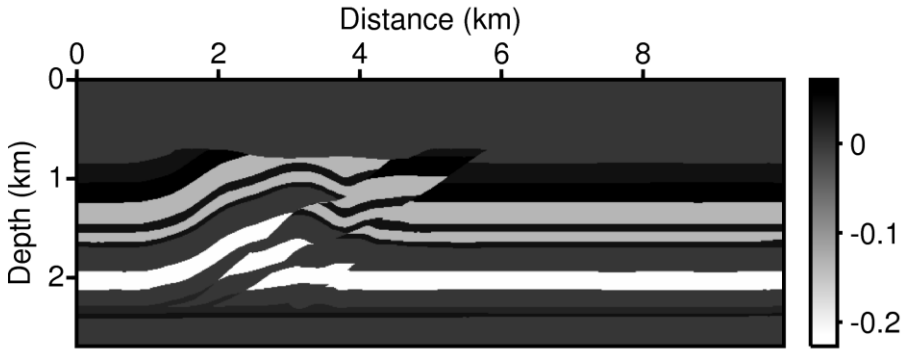

(c)

Figure 14. Overthrust VTI model set: (a) P-wave, (b) epsilon, and (c) delta models

Summary of the information of the synthetic data	
Domain size	10,000m × 2,700m
Number of shots	100 (interval: 100m)
Number of receivers	1000 (fixed, interval: 12.5m)
Modeling scheme	Staggered-grid FDM
Modeling grid size	10.0 m
Source wavelet	First derivative of Gaussian function
Peak frequency	25 Hz
Recording Time	10.0 sec
Time sampling interval	1 ms

Table 4. Summary of the information of the generated time-domain synthetic dataset using the Overthrust parameter set.

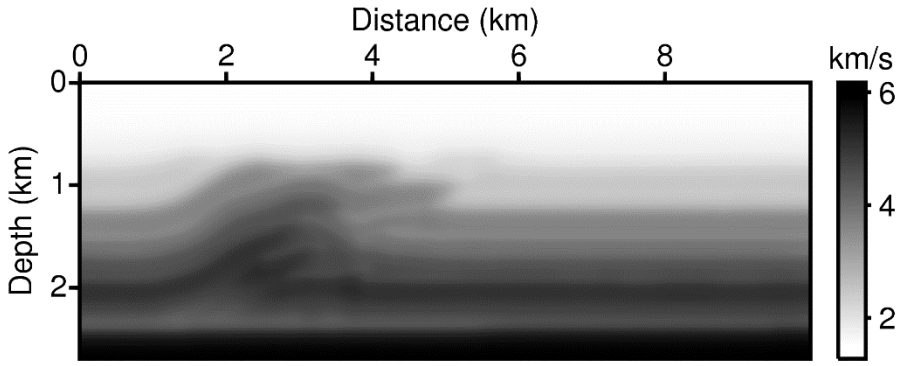

(a)

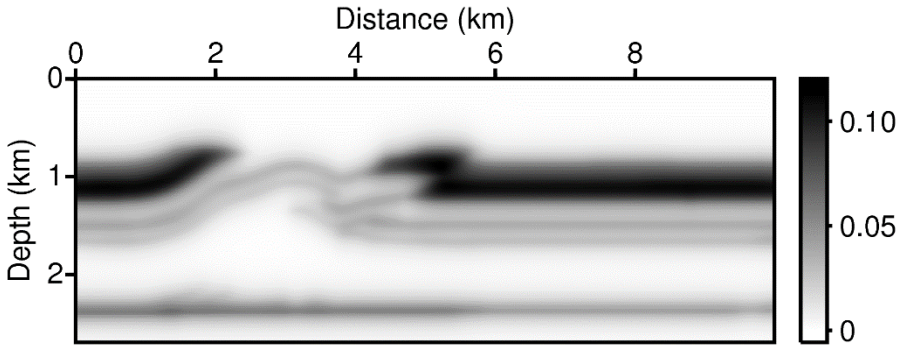

(b)

Figure 15. The initial (a) smoothed P-wave velocity model and (b) smoothed epsilon model

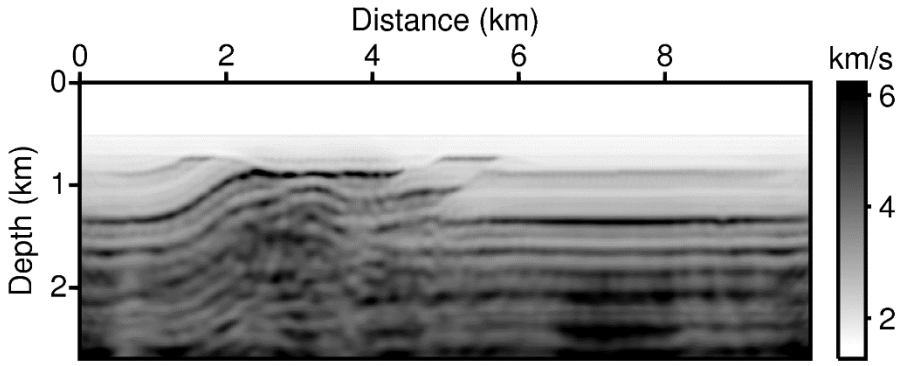

Figure 16. Inverted P-wave velocity model using the conventional isotropy acoustic wave equation

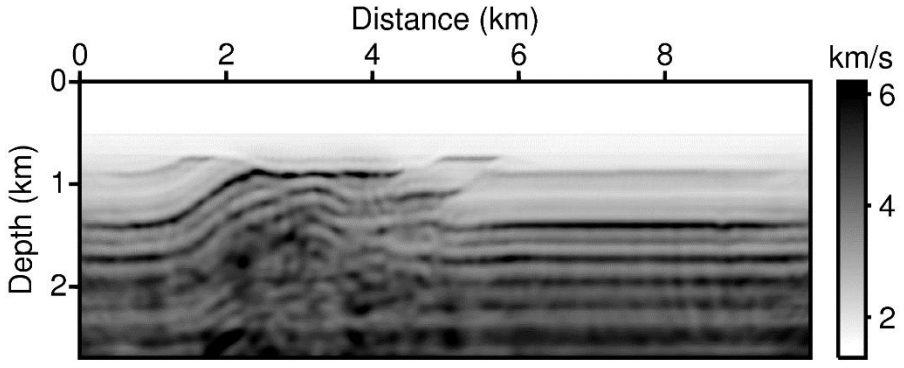

(a)

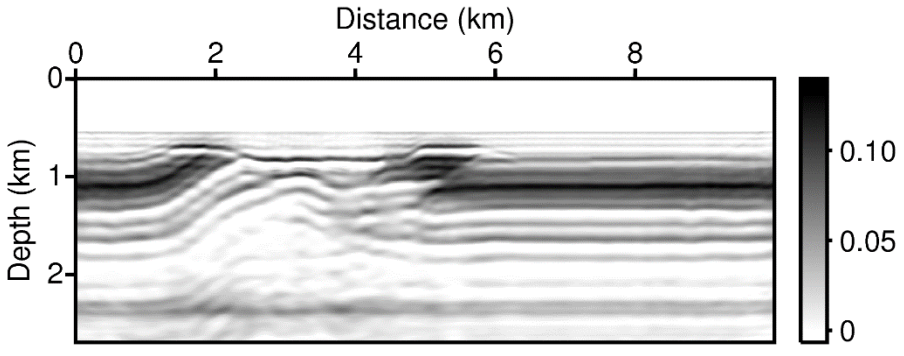

(b)

Figure 17. Inverted model using the pseudo-acoustic wave equation in case 1:

(a) P-wave velocity model and (b) epsilon model

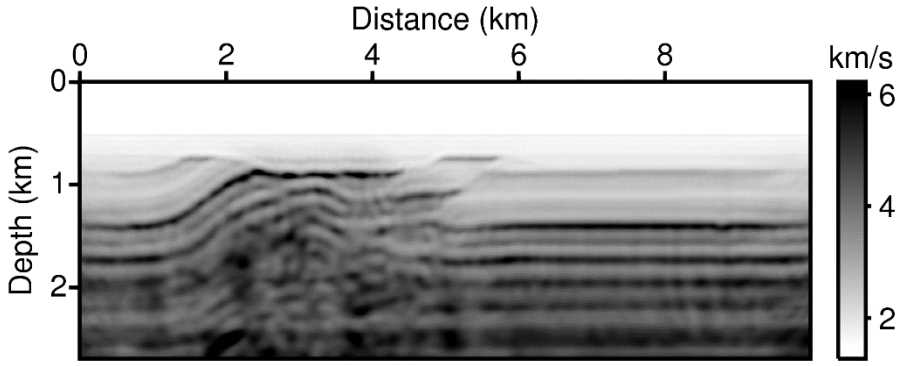

Figure 18. Inverted P-wave velocity model using the pseudo-acoustic wave equation in case 2

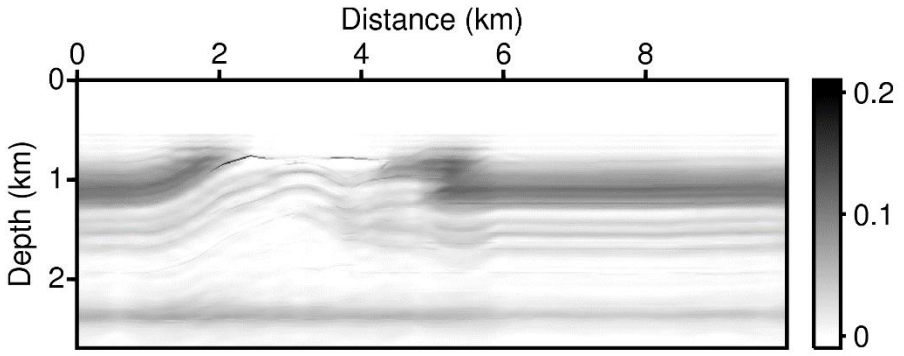

Figure 19. Inverted epsilon model using the pseudo-acoustic wave equation in case 3

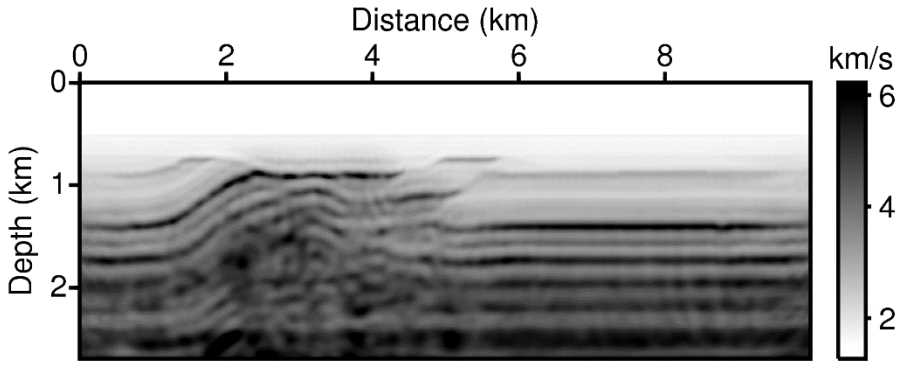

(a)

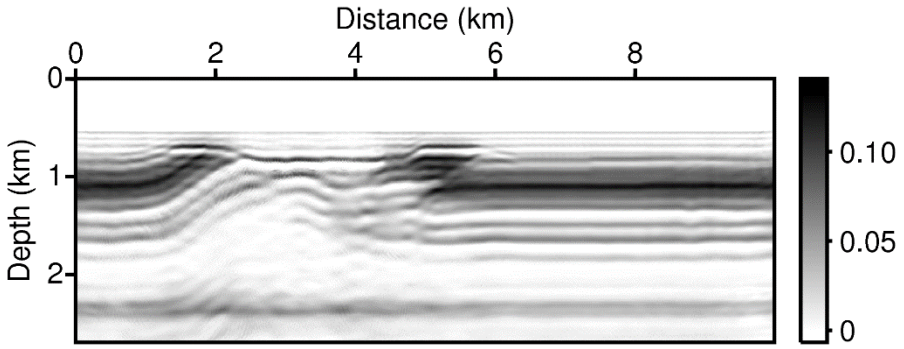

(b)

Figure 20. Inverted model using the pseudo-acoustic wave equation in case 4: (a) P-wave velocity model and (b) epsilon model

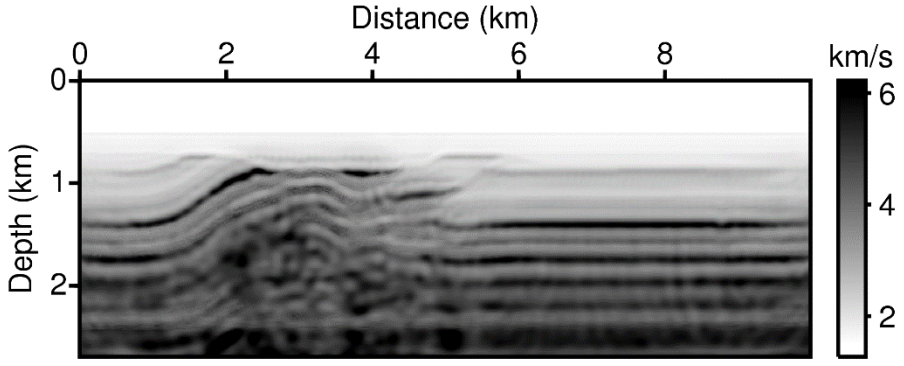

Figure 21. Inverted P-wave velocity model using the pseudo-acoustic wave equation in case 5

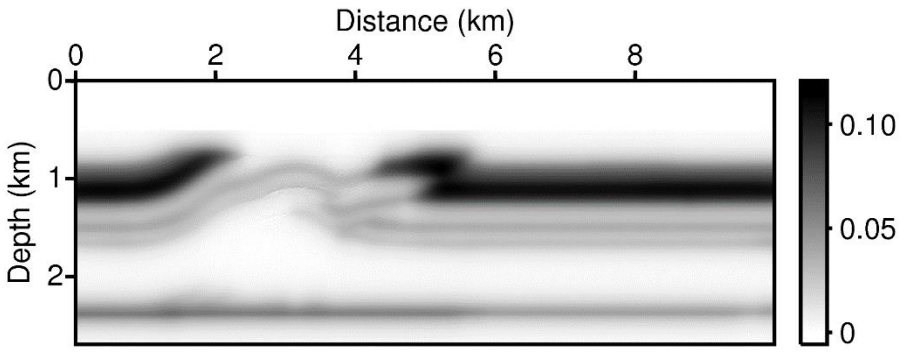

Figure 22. Inverted epsilon model using the pseudo-acoustic wave equation in case 6

	Inverted P-wave velocity model (Isotropy)	**Inverted P-wave velocity model (Anisotropy)**	**Inverted epsilon model (Anisotropy)**
Case 1	14.20239	11.98625	91.94218
Case 2	14.20239	12.09950	-
Case 3	-	-	82.15388
Case 4	14.20239	12.89634	91.13158
Case 5	14.20239	13.51309	-
Case 6	-	-	87.02678

Table 5. The model misfits using the pseudo-acoustic wave equation

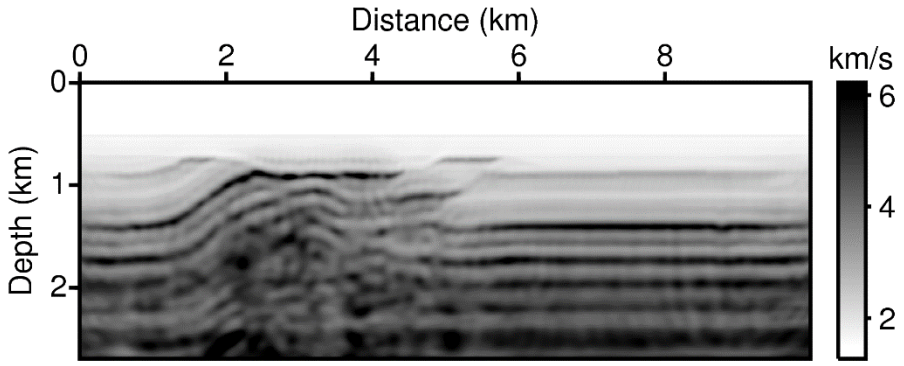

(a)

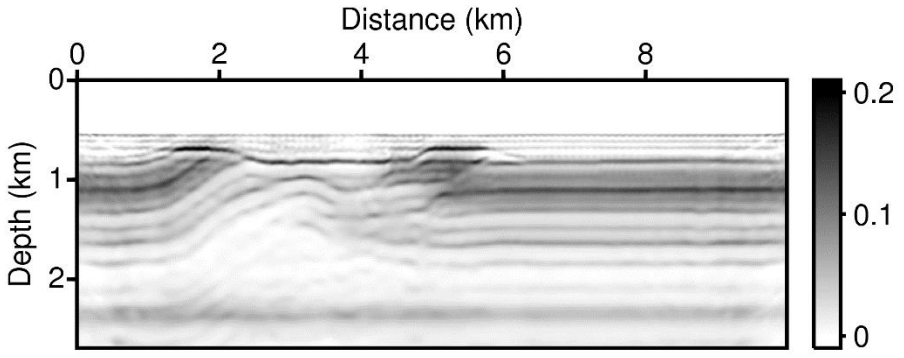

(b)

Figure 23. Inverted model using the pure-acoustic wave equation in case 1: (a) P-wave velocity model and (b) epsilon model

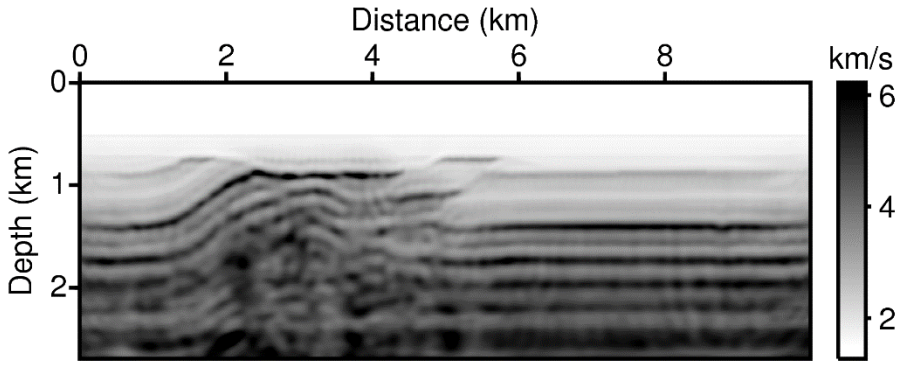

Figure 24. Inverted P-wave velocity model using the pure-acoustic wave equation in case 2

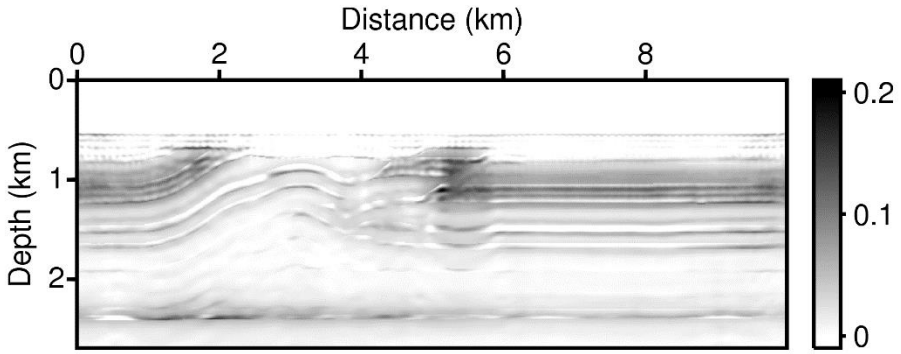

Figure 25. Inverted epsilon model using the pure-acoustic wave equation in case 3

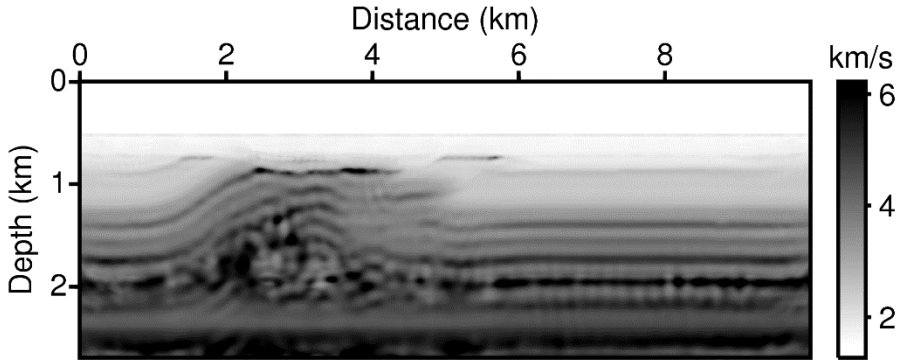

(a)

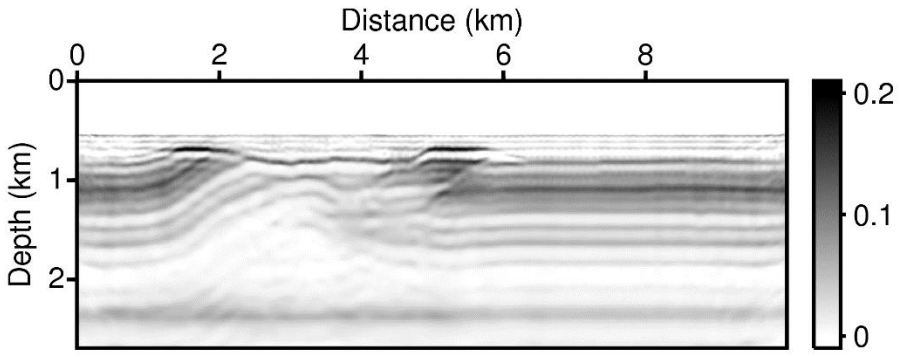

(b)

Figure 26. Inverted model using the pure-acoustic wave equation in case 4: (a) P-wave velocity model and (b) epsilon model

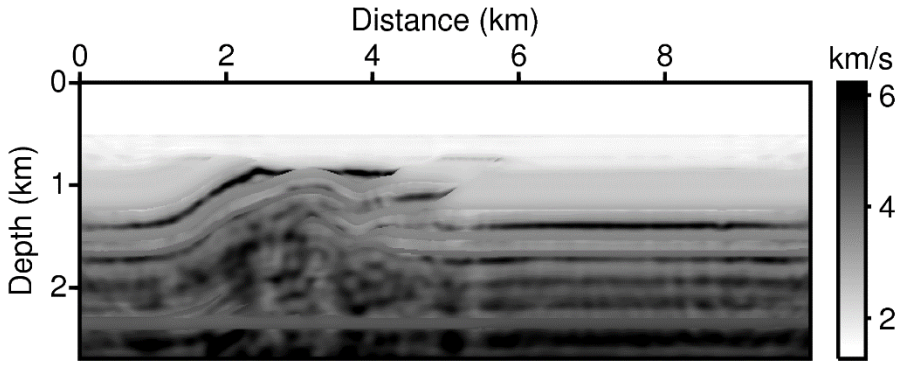

Figure 27. Inverted P-wave velocity model using the pure-acoustic wave equation in case 5

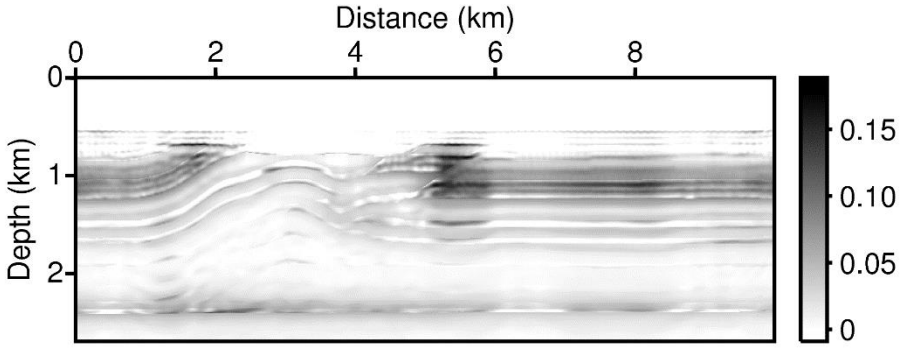

Figure 28. Inverted Epsilon model using the pure-acoustic wave equation in case 6

	Inverted P-wave velocity model (Isotropy)	Inverted P-wave velocity model (Anisotropy)	Inverted epsilon model (Anisotropy)
Case 1	14.20239	13.80213	108.14380
Case 2	14.20239	14.02429	-
Case 3	-	-	95.80306
Case 4	14.20239	11.74118	102.78800
Case 5	14.20239	11.64559	-
Case 6	-	-	97.50259

Table 6. The model misfits using the pure-acoustic wave equation

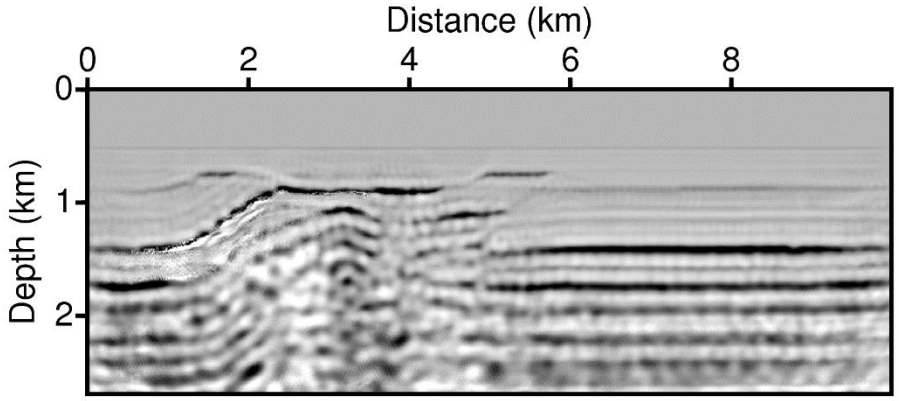

(a)

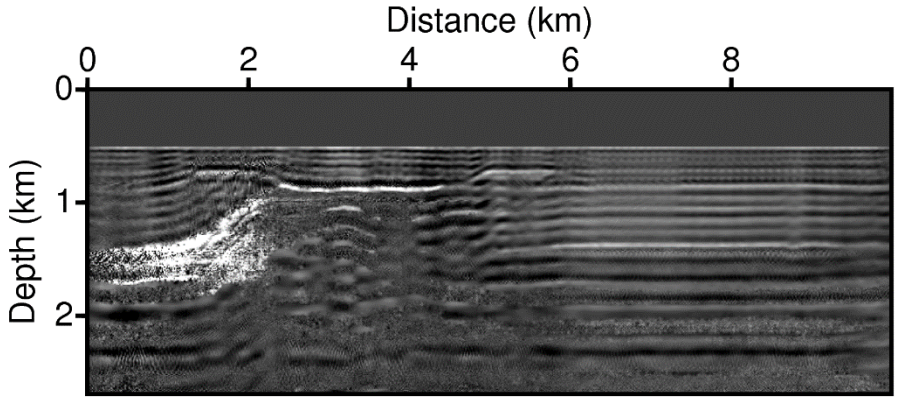

(b)

Figure 29. The gradient direction of (a) the P-wave velocity model and (b) the epsilon using the pseudo-acoustic wave equation in case 4

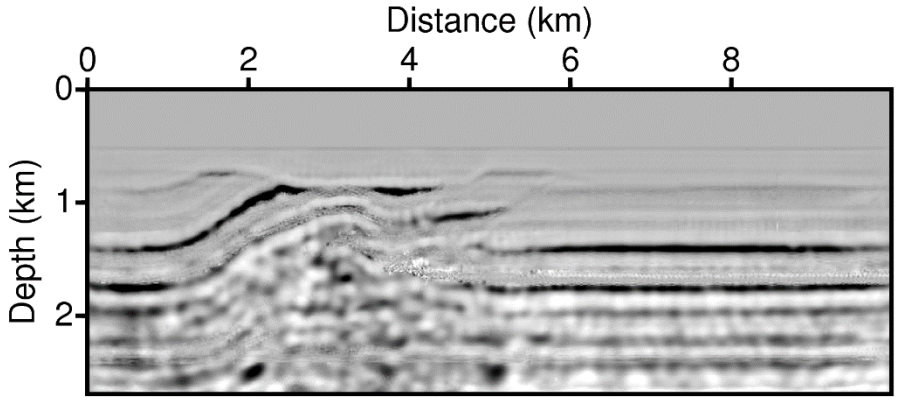

Figure 30. The gradient direction of the P-wave velocity model using the pseudo-acoustic wave equation in case 5

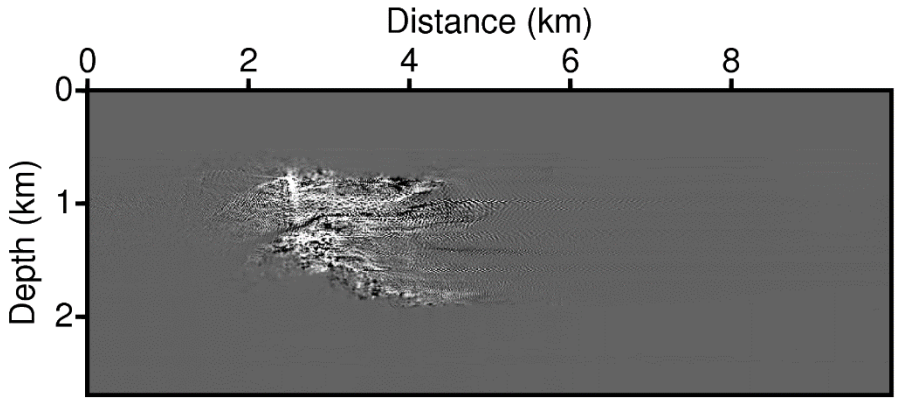

Figure 31. The gradient direction of the epsilon model using the pseudo-acoustic wave equation in case 6

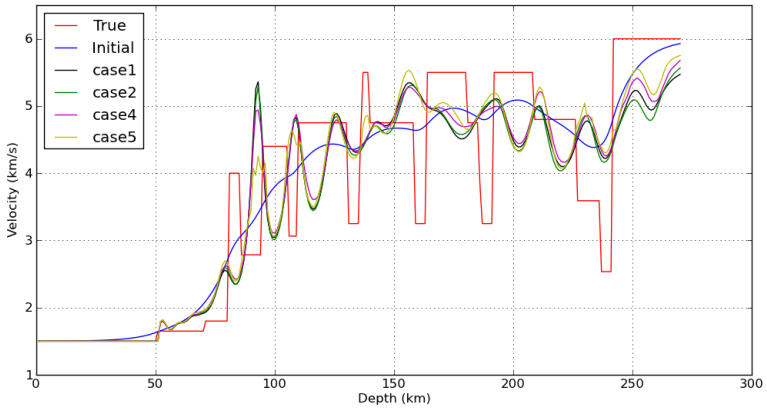

Figure 32. The depth profiles of the P-wave velocity model using the pseudo-acoustic wave equation at 3km from the left edge

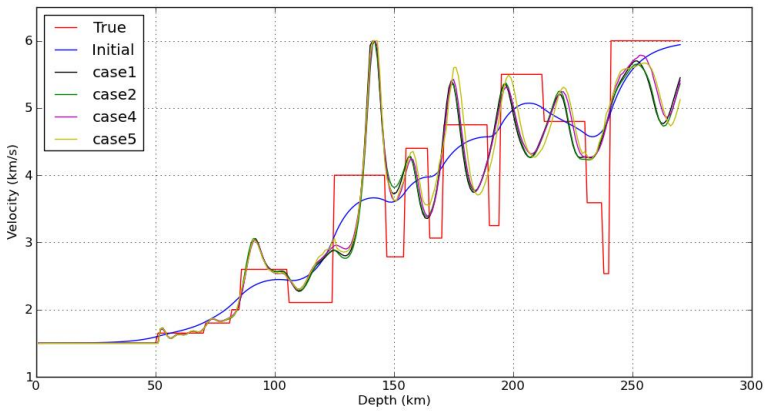

Figure 33. The depth profiles of the P-wave velocity model using the pseudo-acoustic wave equation at 7km from the left edge

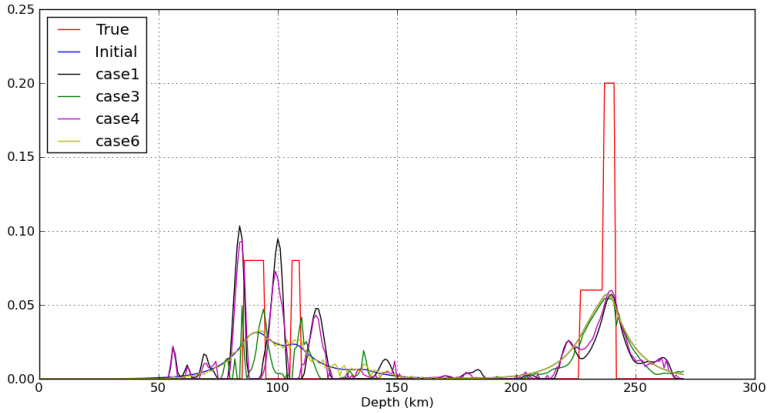

Figure 34. The depth profiles of the epsilon model using the pseudo-acoustic wave equation at 3km from the left edge

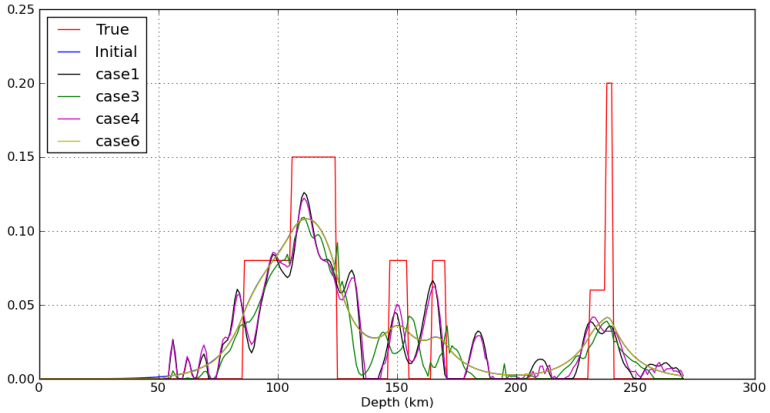

Figure 35. The depth profiles of the epsilon model using the pseudo-acoustic wave equation at 7km from the left edge

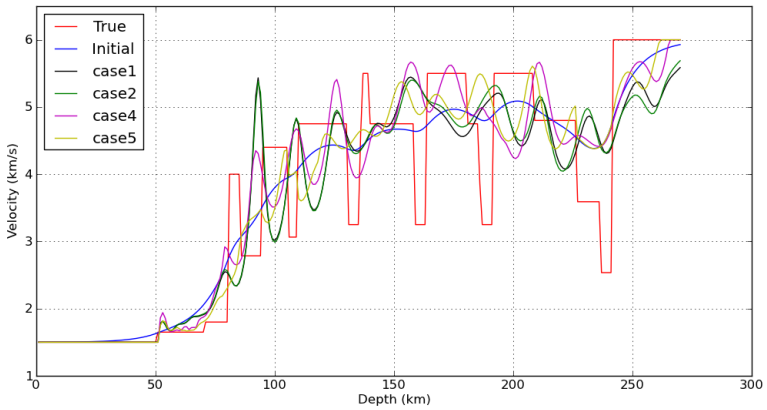

Figure 36. The depth profiles of the P-wave velocity model using the pure-acoustic wave equation at 3km from the left edge

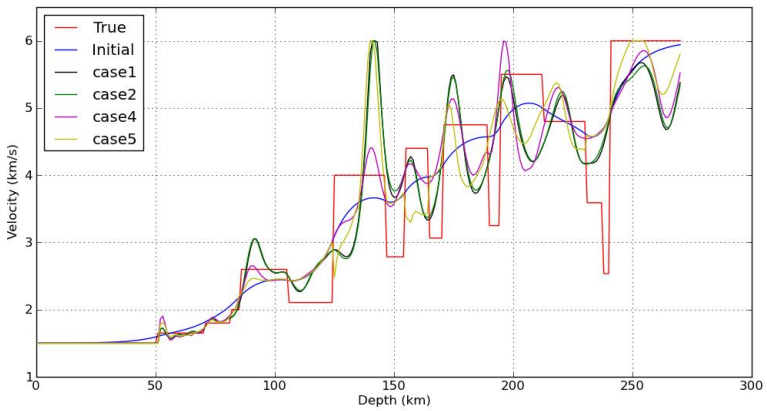

Figure 37. The depth profiles of the P-wave velocity model using the pure-acoustic wave equation at 7km from the left edge

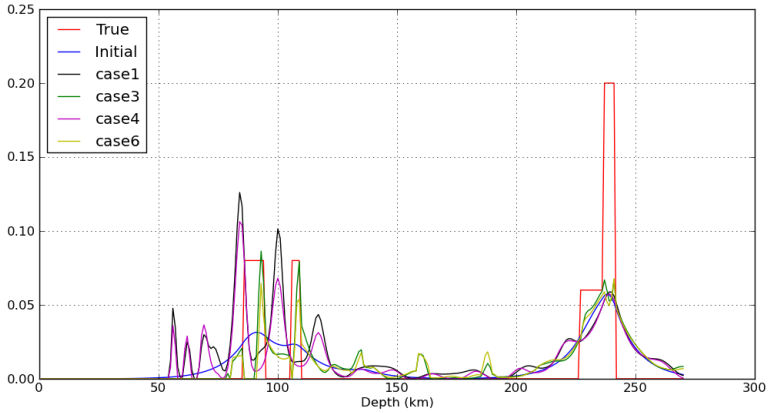

Figure 38. The depth profiles of the epsilon model using the pure-acoustic wave equation at 3km from the left edge

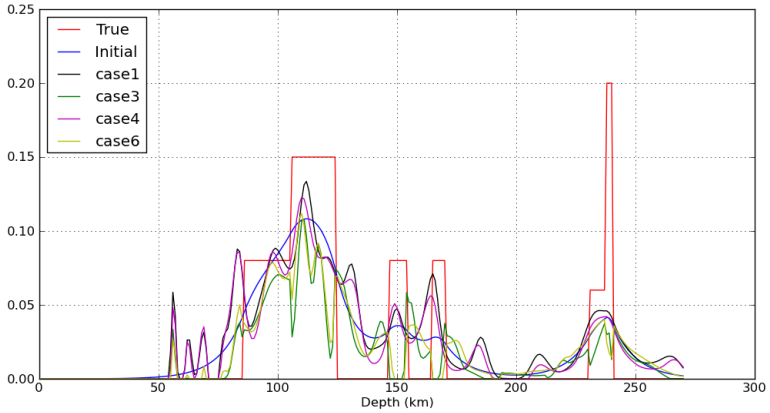

Figure 39. The depth profiles of the epsilon model using the pure-acoustic wave equation at 3km from the left edge

The experiments using synthetic datasets generated in the time-domain present insufficient results compared to the frequency-domain synthetic dataset tests. Table 5 and Table 6 show the relative percentage errors that were calculated using equation (3.2.1), and we can observe that the P-wave velocity model from both of the proposed algorithms has better images than conventional FWI. In cases 4, 5, and 6 using the pseudo-acoustic wave equation, the wavefield would generate shear-wave artifacts, which we could detect in Figure 20, Figure 21, and Figure 22. To specifically inspect the shear-wave artifacts, we present the gradient directions of the P-wave velocity model and the epsilon model in Figure 29, Figure 30, and Figure 31. Figure 29and Figure 30 show that the shear-wave artifacts occurred in some layers, and Figure 31 shows that serious artifacts occurred in complex reverse fault layers. Although the gradient direction of the epsilon model in case 4 is better than that in case 6, the epsilon model misfits of case 6 are lower than those of case 4. Because the gradient direction of case 6 has artifacts with large amplitudes, case 6 only updated the artifacts area, and the other domains were not updated during the waveform inversion. Consequently, in case 6, the domain, except for the part where artifacts occurred, exhibits little difference between the inverted model and the initial model. The depth profiles of the parameters are displayed in Figure 32 to Figure 39.

3.4 Why we consider the anisotropy parameters (BP TTI Model)

The conventional frequency-domain waveform inversion generally considers a single parameter for example, a p-wave. If we consider the anisotropy factors when we perform the waveform inversion, however, we would obtain results that are closer to the correct answer. To verify this hypothesis, we inverted the P-wave velocity model using the conventional acoustic wave equation and the pure-acoustic wave equation for synthetic data created by the "BP Exploration Operation Company". The inverted P-wave velocity models would establish why we consider the anisotropy factors when we perform the waveform inversion.

Specific details of the model parameters of the synthetic datasets are presented in Figure 40, and the modeling details are presented in Table 7. To test these synthetic data, we need to reconstruct the model parameters. First, the modeling grid interval needs to be increased because the number of total nodal points of the original model is 22,685,393.0, which is too large to solve the impedance matrix with our computing abilities. For this reason, we resized the model parameters to match the 50 m grid interval. Due to the spacing, we used the maximum frequency of the source wavelet of 8 Hz. Our initial P-wave velocity model for the two waveform inversion algorithms is the smoothed model illustrated in Figure 41.a. We assumed that the domain was VTI media; in fact, synthetic data were generated in a TTI media environment, and we used tiny smoothed epsilon and delta models as the initial models during the pure-acoustic waveform inversion. Both are illustrated in Figure 41. b and c.

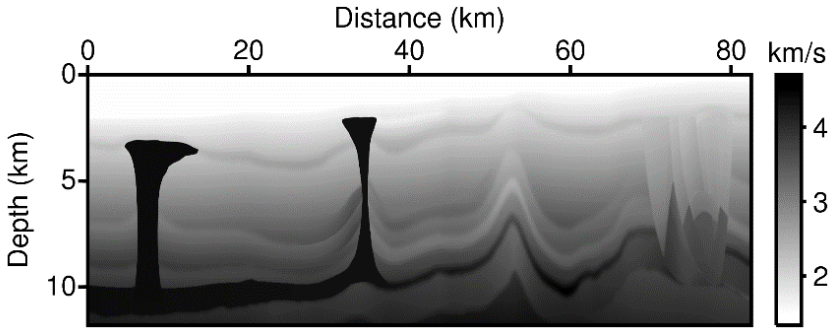
Distance (km)
0
20
40
60
80
km/s
Depth (km)
0
5
10
4
3
2

(a)

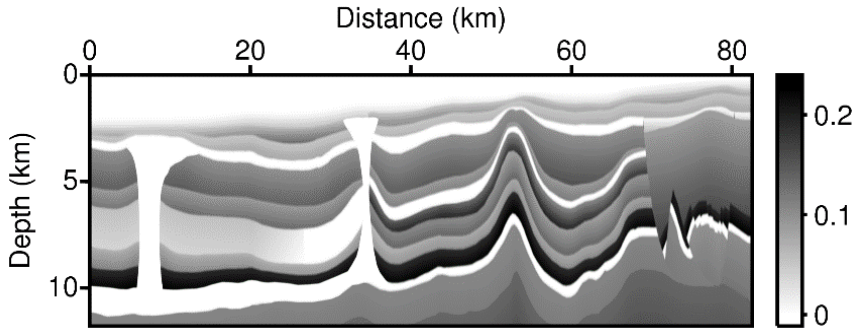
Distance (km)
0
20
40
60
80
Depth (km)
0
5
10
0.2
0.1
0

(b)

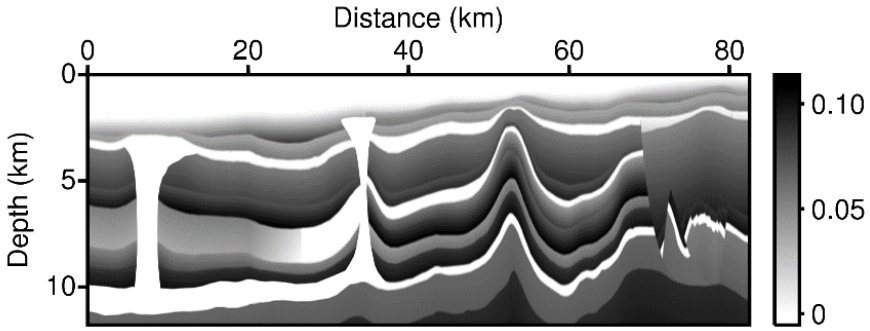
Distance (km)
0
20
40
60
80
Depth (km)
0
5
10
0.10
0.05
0

(c)

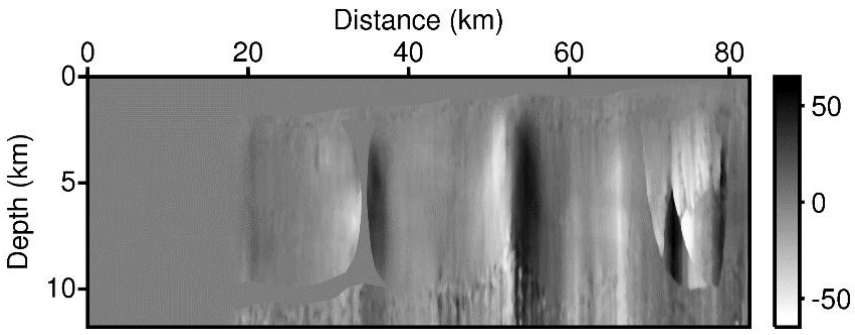

(d)

Figure 40. The true model of the BP TTI model, (a)P-wave velocity model, (b)epsilon model, (c)delta model, and (d)theta model

Summary of the information of the synthetic data	
Domain size	78,725m × 11,256m
Minimum offset length	37.5m
Maximum offset length	10,025m
Number of shots	1641 (interval: 50m)
Number of receivers	800 (Streamer, channel separation: 12.5m)
Recording Time	9.2sec
Modeling grid size	6.25m

Table 7. Summary of the information of the BP TTI synthetic dataset

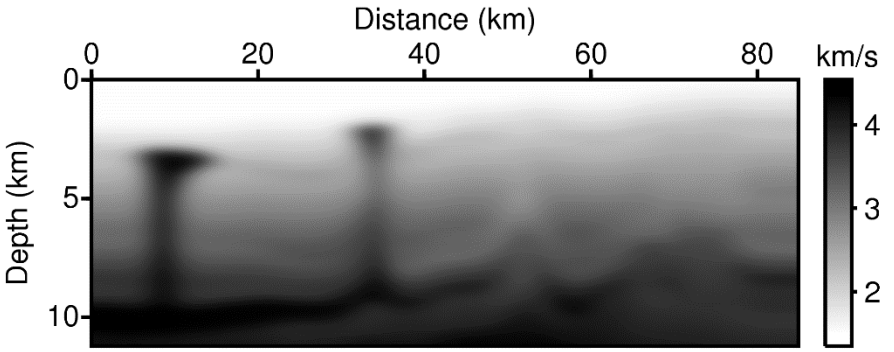

(a)

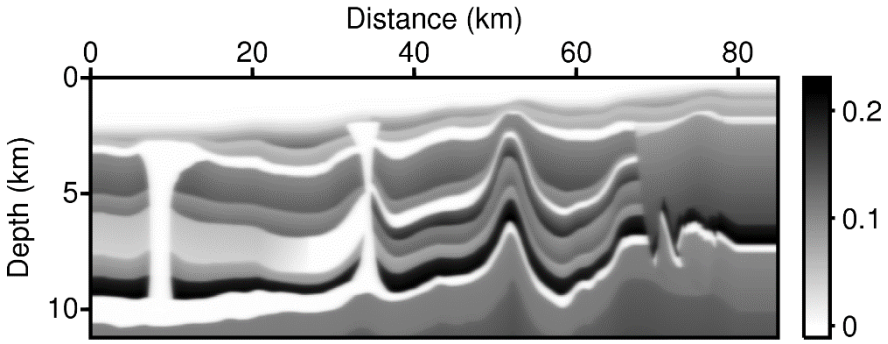

(b)

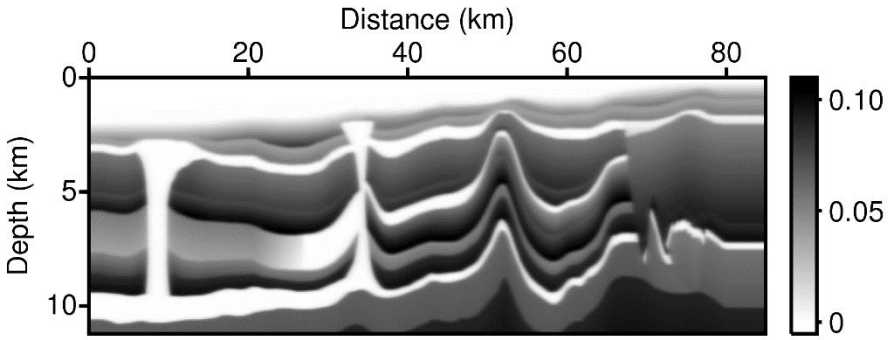

(c)

Figure 41. (a) The smoothed initial P-wave velocity model from conventional isotropy waveform inversion and anisotropy waveform inversion, (b) the initial epsilon model, and (c) the initial delta model

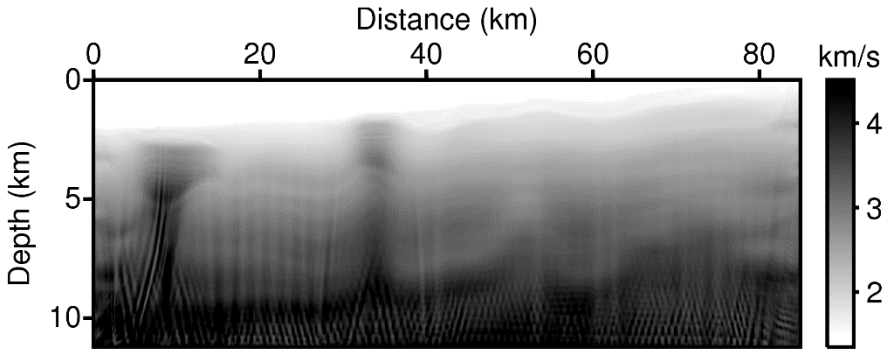

Figure 42. The inverted P-wave velocity model from conventional isotropy waveform inversion.

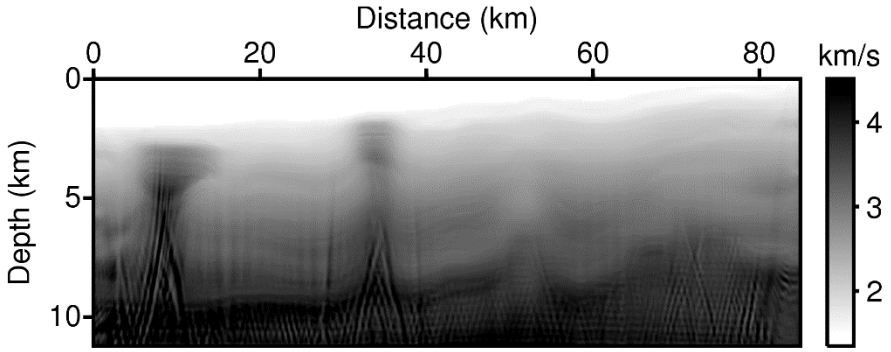

Figure 43. The inverted P-wave velocity model from anisotropy waveform inversion

As shown in Figure 42, the inverted P-wave velocity model from the conventional isotropy wave equation has some vertical directional artifacts between salt pillars. In Figure 43, however, the inverted P-wave velocity model from the pure-acoustic wave equation, which considered almost true epsilon and delta values, more clearly show the image, and complex layers located on the right-side of domain are more reconstructed than in Figure 42. In addition, the relative percentage error of the inverted P-wave velocity model for conventional isotropy FWI is 4.7057%, whereas for anisotropy FWI, it is 4.3126%. The anisotropy parameters are important factors that characterize the feature of subsurface rock. From the above results, we verified that the anisotropy parameters are the important factor for the waveform inversion of

the P-wave velocity. Because of the consideration of the anisotropy parameters, the propagation of P-waves is more accurate in anisotropic media.

Unfortunately, however, this experiment was far from realistic conditions because it is impossible to guess the initial anisotropy model as in Figure 41 (b) and (c). Nevertheless, we proved that the P-wave velocity would be reconstructed well if the anisotropy parameters such as epsilon and delta are obtained from well logging data or other seismic data.

Chapter 4 Conclusions

We developed a multiparameter FWI in the frequency-domain using the pseudo-acoustic and pure-acoustic wave equations. First, we simulated the radiation patterns of the dominant parameter and of anisotropy parameters such as P-wave, epsilon, and delta. The experimental results revealed different aspects for pseudo-acoustic waves and pure-acoustic waves. In the non-elliptical case, the radiation pattern of the pseudo-acoustic wave could not be detected because the amplitude of shear-wave artifacts was larger than the amplitude of the partial derivative wavefield. In the elliptical case, however, shear-wave artifacts were not generated, and we could verify the scattering motion of P-wave and anisotropy parameters. The radiation pattern of the dominant parameter and anisotropy parameters of the pseudo-acoustic wave spread mainly in horizontal directions. The difference in the dominant and anisotropy parameters occurred in the central part of the wavefield. The radiation patterns of the dominant parameter and anisotropy parameters for pure-acoustic wave also have different aspects. In particular, the scattering motion of epsilon is highly sensitive to the incidence angles. The trade-off effect, which is called crosstalk, occurred when the radiation patterns of each parameter overlapped. Based on the experiments, we expected that the pure-acoustic wave is more suitable than the pseudo-acoustic wave considering realistic rock environments. Second, to verify the performance of both proposed algorithms, we tested both algorithms using synthetic data generated using same wave equation and modeling scheme. Based on the experimental, we have confidence that both algorithms performed well. Additionally, we detected the cross-talk effect when updating the parameters simultaneously. Third, we

generated synthetic data in the time-domain using the elastic wave equation. We established 6 cases of the initial models and updating strategies. Thekey result of the experiment is that both algorithms performed better than conventional isotropy FWI. From analyzing the results of both algorithms, it is difficult to say which algorithm is better. If the initial model of epsilon is true, the P-wave velocity model has to be close to the true velocity model. Unlike our expectations, however, both algorithms in cases 1 and 2 showed that the simultaneous updating strategy has a lower model misfit than case 2. Even if the difference of misfits of both algorithms is 0.2%, these results need to be further enhanced and analyzed. Nevertheless, in comparing case 1 and case 3, the epsilon model is well reconstructed for both algorithms. The difference of cases 1 to 3 and cases 4 to 6 is the presence or absence of the delta. There was no significant difference between the presence and absence of delta. However, when using the pseudo-acoustic wave equation, in cases 4 to 6, the gradient directions were contaminated by shear-wave artifacts and the contaminated gradient directions caused unexpected results. Additionally, in terms of the relative percentage errors, we could not easily decide which one is better. However, considering the realistic rock environment, FWI using the pure-acoustic wave equation is more suitable than using the pseudo-acoustic wave equation. As Thomsen (1986) says, the epsilon value of 'the Mesaverde (4903) mudshale' is 0.034 and the delta is 0.211, the epsilon value of 'the Mesaverde (5501) clayshale is 0.334 and the delta is 0.730, and the epsilon value of 'the Mesaverde (7888.4) sandstone' is 0.033 and the delta is 0.04. Like this example, many rocks have delta values that are larger than the epsilon values. Although in some cases the results of the time-domain synthetic data test showed that the use of pseudo-acoustic wave equation is better than the use of the pure-acoustic wave equation, we have to invert the parameters to avoid unwanted signals.

Although the performance of the two algorithms is a topic for a later discussion, the remarkable discovery of this study is that the results of all 6 cases for both algorithms indicate that FWI considering the anisotropy parameters has better outcomes than conventional isotropy FWI. Finally, we also applied both algorithms to officially provided synthetic data for the "BP TTI Model". Through this work, we proved once again that the anisotropic multiparameter FWI can obtain a better P-wave velocity model than the previous single-parameter FWI by using the initial anisotropy model that is closer to the true.

The future research plans are as follows: First, minimizing the cross-talk effect among the parameters. According to the multiparameter FWI, eliminating the effect of interference between variables is an important task. Second, enhancing the algorithms. Neither of the developed algorithms have yet been applied to techniques such as the regularization of the objective function; using other objective functions, for example, L1-norm, Logarithmic, and Huber; and applying other scaling method, for instance, full-Hessian matrix, approximated Hessian matrix, and so on. Finally, test real data. We need to compare the performance of the conventional method and the new method, and we need to make a comparison between subsurface images from the conventional method and from the proposed method using RTM. Additionally, we need to analyze SDCIG and ADCIG and determine which images are flatter.

REFERENCES

Alkhalifah, Tariq. "An acoustic wave equation for anisotropic media."*Geophysics* 65.4 (2000): 1239-1250.

Ben-Hadj-Ali, Hafedh, Stéphane Operto, and Jean Virieux. "Velocity model building by 3D frequency-domain, full-waveform inversion of wide-aperture seismic data." *Geophysics* 73.5 (2008): VE101-VE117.

Brossier, Romain, Stéphane Operto, and Jean Virieux. "Seismic imaging of complex onshore structures by 2D elastic frequency-domain full-waveform inversion." *Geophysics* 74.6 (2009): WCC105-WCC118.

Bunks, Carey, et al. "Multiscale seismic waveform inversion." *Geophysics* 60.5 (1995): 1457-1473.

Choi, Yunseok, Dong-Joo Min, and Changsoo Shin. "Two-dimensional waveform inversion of multi-component data in acoustic-elastic coupled media." *Geophysical Prospecting* 56.6 (2008): 863-881.

Chu, Chunlei, Brian K. Macy, and Phil D. Anno. "Approximation of pure acoustic seismic wave propagation in TTI media." *Geophysics* 76.5 (2011): WB97-WB107.

Duveneck, Eric, et al. "Acoustic VTI wave equations and their application for anisotropic reverse-time migration." *SEG Technical Program Expanded Abstracts 2008*. Society of Exploration Geophysicists, 2008. 2186-2190.

Fletcher, Robin P., Xiang Du, and Paul J. Fowler. "Reverse time migration in tilted transversely isotropic (TTI) media." *Geophysics* 74.6 (2009): WCA179-

WCA187.

Gauthier, Odile, Jean Virieux, and Albert Tarantola. "Two-dimensional nonlinear inversion of seismic waveforms: Numerical results." *Geophysics* 51.7 (1986): 1387-1403.

Gholami, Yaser, et al. "Which parameterization is suitable for acoustic vertical transverse isotropic full waveform inversion? Part 1: Sensitivity and trade-off analysis." *Geophysics* 78.2 (2013): R81-R105.

Gholami, Yaser, et al. "Which parameterization is suitable for acoustic vertical transverse isotropic full waveform inversion? Part 2: Synthetic and real data case studies from Valhall." *Geophysics* 78.2 (2013): R107-R124.

Guitton, Antoine, and William W. Symes. "Robust inversion of seismic data using the Huber norm." *Geophysics* 68.4 (2003): 1310-1319.

Kim, Jeong Ho, and Seung Jo Kim. "Multifrontal solver combined with graph partitioners." *AIAA journal* 37.8 (1999): 964-970.

Kim, Youngseo, et al. "An algorithm for 3D acoustic time-Laplace-Fourier-domain hybrid full waveform inversion." *Geophysics* 78.4 (2013): R151-R166.

Kim, Youngseo, et al. "Acceleration of stable TTI P-wave reverse-time migration with GPUs." *Computers & Geosciences* 52 (2013): 204-217.

Lailly, Patrick. "The seismic inverse problem as a sequence of before stack migrations." *Conference on inverse scattering: theory and application*. Society for Industrial and Applied Mathematics, Philadelphia, PA, 1983.

Lee, Ho-Yong, et al. "Frequency-domain elastic full waveform inversion for VTI media." *Geophysical Journal International* 183.2 (2010): 884-904.

Mora, Peter. "Nonlinear two-dimensional elastic inversion of multioffset seismic data." *Geophysics* 52.9 (1987): 1211-1228.

Operto, S., et al. "Quantitative imaging of complex structures from dense wide-aperture seismic data by multiscale traveltime and waveform inversions: a case study." *Geophysical prospecting* 52.6 (2004): 625-651.

Plessix, René-Édouard. "Three-dimensional frequency-domain full-waveform inversion with an iterative solver." *Geophysics* 74.6 (2009): WCC149-WCC157.

Pratt, R. Gerhard, Changsoo Shin, and G. J. Hick. "Gauss–Newton and full Newton methods in frequency–space seismic waveform inversion. "*Geophysical Journal International* 133.2 (1998): 341-362.

Shin, Changsoo, Seonghyung Jang, and Dong-Joo Min. "Improved amplitude preservation for prestack depth migration by inverse scattering theory."*Geophysical prospecting* 49.5 (2001): 592-606.

Shin, Changsoo, and Dong-Joo Min. "Waveform inversion using a logarithmic wavefield." *Geophysics* 71.3 (2006): R31-R42.

Shin, Changsoo, Sukjoon Pyun, and J. Bednar. "Comparison of waveform inversion, part 1: conventional wavefield vs logarithmic wavefield." *Geophysical Prospecting* 55.4 (2007): 449-464.

Shipp, Richard M., and Satish C. Singh. "Two-dimensional full wavefield inversion of wide-aperture marine seismic streamer data." *Geophysical Journal International* 151.2 (2002): 325-344.

Sirgue, Laurent, and R. Gerhard Pratt. "Efficient waveform inversion and imaging: A strategy for selecting temporal frequencies." *Geophysics* 69.1

(2004): 231-248.

Sirgue, L., J. T. Etgen, and U. Albertin. "3D frequency domain waveform inversion using time domain finite difference methods." *70th EAGE Conference & Exhibition*. 2008.

Tarantola, Albert. "Inversion of seismic reflection data in the acoustic approximation." *Geophysics* 49.8 (1984): 1259-1266.

Thomsen, Leon. "Weak elastic anisotropy." *Geophysics* 51.10 (1986): 1954-1966.

Trefethen, Lloyd N., and David Bau III. *Numerical linear algebra*. Vol. 50. Siam, 1997.

Tsvankin, Ilya, Klaus Helbig, and Sven Treitel. "Seismic signatures and analysis of reflection data in anisotropic media." (2001).

Wang, Zhijing. "Seismic anisotropy in sedimentary rocks, part 2: Laboratory data." *Geophysics* 67.5 (2002): 1423-1440.

Zhang, Yu, and Houzhu Zhang. "A stable TTI reverse time migration and its implementation." *2009 SEG Annual Meeting*. Society of Exploration Geophysicists, 2009.

초 록

완전파형역산을 진행하면서 좀 더 정확한 지하속도모델을 얻기 위해서는 정확한 파동의 묘사가 필요하다. 실제 지하매질은 이방성 형태로 존재하며 기존의 완전파형역산은 지하매질을 등방성 매질로 가정하고 수행하기 때문에 정확한 파의 거동 묘사가 불가능하다. 이는 지하속도모델을 얻는 과정에서 충분치 못한 결과를 얻을 것이다.

수치적으로 정확한 파동 전파를 구현하기 위하여 우리는 Fletcher et al. 과 Chu et al. 이 제안한 유사 파동 방정식과 순수 음향 파동 방정식을 도입하였다. 두 방정식은 식의 형태가 크게 다르기 때문에 완전파형역산 알고리즘에 적용한다면 성능의 차이가 있을 것으로 생각된다. 다 변수 완전파형역산에서 중요한 고려 사항 중 하나는 변수들의 방사 형태이다. 변수들의 방사 형태는 편미분 파동장을 구하는 방식으로 구할 수 있으며, 변수들의 방사 형태들은 서로 영향을 주지 않는 방향으로 설정되는 것이 다 변수 완전파형역산의 결과에 유리하다고 많이 알려져 있다.

우리는 주파수 영역에서 두 방정식을 구현해 보았고, 시간 영역에서 두 방정식의 P파, Epsilon, 그리고 Delta값의 방사 형태를 구해보았다. 두 알고리즘의 동작 유/무와 가능성을 판단하기 위하여, 인공합성자료를 동일한 방정식과 모델링 방법을 주파수 영역에서 만들어 실험해 보았다. 좀 더 현실적인 상황을 고려하여, 시간 영역에서 탄성파 방정식을 사용한 해상 환경을 가정한 인공 합성자료를 만들어 두 알고리즘을 적용해 보았다. 총 6가지 경우의

시작 모델과 업데이트 방식을 설정하여 실험하였다. 또한 기존 단일 변수 완전파형역산도 진해하였고, 실제 모델 값과 역산된 결과 값 사이의 상대적인 오차를 구하여 기존의 단일 변수 완전파형 역산과의 성능 차이도 계산하였다. 마지막으로, 공식적으로 BP Exploration Operation社 에서 제공한 2차원 경사진 횡등방성매질 인공합성자료에 대하여도 이방성 다 변수 완전파형역산을 진행하여 이방성 매질의 중요성을 확인하였다.

주요어 : 주파수 영역 완전 파형 역산, 이방성 변수, 유사 음향 파동 방정식, 순수 음향 파동 방정식

학번 : 2013-23186